

BAMS



A SIP of ICY AIR

SPICULE Investigates Secondary Ice Processes in Cumulus Clouds



Bulletin of
the American
Meteorological Society

Volume 104
Number 10
October 2023

NOWCAST

- 779 **Conference Notebook:** Modeling Smoke Impacts on Air Quality
- 783 **Papers of Note:** Model Bias Correction with Crowdsourcing
- 786 **Parcels:** Understanding Clouds with Machine Learning; A Natural Protection for Pacific Coral; Website Maps NYC Tree Shade; Arctic Seafloor Influences Surface Ice; The Lingering Storms of Saturn

DEPARTMENTS

- 770 **Precursors**
- 839 **Call for Papers**
- 840 **Meetings and Events**
- 849 **Outlooks**

45 BEACON

- 823 **Policy:** A Fresh Look at the Weather Enterprise Two Decades After the "Fair Weather" Report, by Keith L. Seitter, Mary M. Glackin, and Paul A. T. Higgins
- 827 **Member Spotlight:** Richard Rotunno
- 828 **Meet the AMS:** Jane Foley, Peer Review Support Assistant
- 829 **Fellowships:** Julian Arnheim, AMS Graduate Fellowship
- 829 **Do Points:** Seeking input on geoscience innovation and entrepreneurship
- 830 **Lightning Round:** What is the most important thing you've learned practicing your profession?
- 832 **Obituaries:** Gerald J. Dittberner
- 833 **In Memoriam**
- 834 **Clear Skies Ahead:** Kelly Núñez Ocasio
- 826 **Living on the Real World, with William H. Hooke:** K-12 Climate Science Education: The Worldwide Picture



Richard Rotunno

"Aviation initiated my interest in meteorology. As a sophomore during my undergraduate studies in electrical engineering, I started flying and wanted to learn more about clouds and how they impact pilot safety. Continuing my education to complete a Ph.D. in atmospheric science was largely stimulated by inspiration from Al Cooper, one of my graduate advisors at the University of Wyoming."

—Paul Lawson, SPEC Incorporated

PAGE 801

Paul Lawson cycling on the Elephant Rock century ride in eastern Colorado.





Paul Lawson in the cockpit of the SPEC Learjet during a campaign out of the United Arab Emirates in September.

“Given the opportunity, after the Secondary Production of Ice in Cumulus Experiment (SPICULE) we will continue to participate in international field projects, collect and analyze data, and publish results.”

— Paul Lawson, SPEC Incorporated

PAGE 801

The Secondary Production of Ice in Cumulus Experiment (SPICULE)

R. Paul Lawson, Alexei V. Korolev, Paul J. DeMott, Andrew J. Heymsfield, Roelof T. Bruintjes, Cory A. Wolff, Sarah Woods, Ryan J. Patnaude, Jørgen B. Jensen, Kathryn A. Moore, Ivan Heckman, Elise Rosky, Julie Haggerty, Russell J. Perkins, Ted Fisher, and Thomas C. J. Hill

ABSTRACT: The secondary ice process (SIP) is a major microphysical process, which can result in rapid enhancement of ice particle concentration in the presence of preexisting ice. SPICULE was conducted to further investigate the effect of collision–coalescence on the rate of the fragmentation of freezing drop (FFD) SIP mechanism in cumulus congestus clouds. Measurements were conducted over the Great Plains and central United States from two coordinated aircraft, the NSF Gulfstream V (GV) and SPEC Learjet 35A, both equipped with state-of-the-art microphysical instrumentation and vertically pointing W- and Ka-band radars, respectively. The GV primarily targeted measurements of subcloud aerosols with subsequent sampling in warm cloud. Simultaneously, the Learjet performed multiple penetrations of the ascending cumulus congestus (CuCg) cloud top. First primary ice was typically detected at temperatures colder than -10°C , consistent with measured ice nucleating particles. Subsequent production of ice via FFD SIP was strongly related to the concentration of supercooled large drops (SLDs), with diameters from about 0.2 to a few millimeters. The concentration of SLDs is directly linked to the rate of collision–coalescence, which depends primarily on the subcloud aerosol size distribution and cloud-base temperature. SPICULE supports previous observational results showing that FFD SIP efficiency could be deduced from the product of cloud-base temperature and maximum diameter of drops measured ~ 300 m above cloud base. However, new measurements with higher concentrations of aerosol and total cloud-base drop concentrations show an attenuating effect on the rate of coalescence. The SPICULE dataset provides rich material for validation of numerical schemes of collision–coalescence and SIP to improve weather prediction simulations

KEYWORDS: Aerosols; Climate change; Cloud microphysics; Cumulus clouds; Ice particles; Mixed precipitation

<https://doi.org/10.1175/BAMS-D-21-0209.1>

Corresponding author: R. Paul Lawson, plawson@specinc.com

In final form 5 August 2022

© 2023 American Meteorological Society. This published article is licensed under the terms of the default AMS reuse license. For information regarding reuse of this content and general copyright information, consult the AMS Copyright Policy (www.ametsoc.org/PUBSReuseLicenses).

AFFILIATIONS: Lawson, Woods, and Fisher—SPEC Incorporated, Boulder, Colorado; Korolev and Heckman—Environment and Climate Change Canada, North York, Ontario, Canada; DeMott, Patnaude, Moore, Perkins, and Hill—Colorado State University, Fort Collins, Colorado; Heymsfield, Brientjes, Wolff, Jensen, and Haggerty—National Center for Atmospheric Research, Boulder, Colorado; Rosky—Michigan Technological University, Houghton, Michigan

The production of ice in clouds has a dominant impact on global precipitation. Field and Heymsfield (2015) analyzed *CloudSat* radar data and found that 50% of global precipitation originated from ice particles. It has long been known that pure water can remain unfrozen down to -38°C unless it interacts with an ice nucleating particle (INP) (e.g., Vonnegut 1947). The origin and concentration of INPs and ice particles in cumulus congestus clouds (CuCg) have been the subject of airborne investigations for several decades. For example, airborne measurements dating back to the early 1960s suggest that the concentration of ice particles in cumulus clouds with cloud-top temperatures $\geq \sim -10^{\circ}\text{C}$ is typically orders of magnitude greater than the concentration of INPs at that temperature (Koenig 1963; Braham 1964). The greater concentration of ice particles compared to the concentration of INPs is thought to be due to a secondary ice process (SIP) (Field et al. 2017), which has also been referred to as ice multiplication (Hobbs 1969). Korolev and Leisner (2020) provide a detailed description of six possible SIP mechanisms based on laboratory experiments. It has been shown that the efficiencies of each of the six SIP mechanisms depend on various environmental and microphysical parameters. This is suggestive that the rate of SIP is linked to cloud dynamics and therefore to the cloud type. We also note that shattering of ice particles on probe tips has been shown to produce anomalously high ice particle concentrations. The instruments used in this study have tips and inlets designed to minimize ice particle shattering, and algorithms are incorporated into postprocessing software to reduce the number of artifacts produced by shattering (Lawson 2011; Korolev et al. 2013).

The SPICULE project focused on the SIP mechanism associated with the fragmentation of freezing supercooled large drops (SLDs), which are on the order of hundreds of micrometers to millimeters in diameter. Upon freezing, SLDs have been shown in the laboratory to produce large quantities of small ice particles (Wildeman et al. 2017). Experiments by Lauber et al. (2018) and Keinert et al. (2020) have also shown that freezing drops produce copious tiny particles, but these particles have yet to be identified as ice. Previous airborne measurements have associated anomalously high concentrations of ice particles in CuCg with SLDs formed via the coalescence process (Koenig 1963; Braham 1964; Hobbs and Rangno 1990; Lawson et al. 2015, 2017, 2022, hereafter L22). Other SIP mechanisms have been reported or hypothesized in clouds (see Korolev et al. 2020), but data from SPICULE and previous CuCg investigations indicate that fragmentation of freezing drops (hereafter FFD) is the only active mechanism in moderate-to-strong ($5\text{--}20\text{ m s}^{-1}$) fresh updrafts of growing CuCg (Lawson et al. 2015, 2017; L22). SPICULE and other datasets can be analyzed to determine if additional SIP processes are active. For example, the Hallett–Mossop rime-splintering process (Hallett and Mossop 1974) and ice-to-ice fracturing (Vardiman 1978) process are typically active at later stages in cloud lifetimes (Heymsfield and Willis 2014; L22), but SPICULE focused only on the early (cumulus) stage of ice and precipitation development. Here we refer to the “cumulus”

stage of development in contrast to mature and dissipating stages of development (Byers and Braham 1949).

SPICULE utilized two jet research aircraft working in concert with state-of-the-art microphysical instruments and airborne radars to document the development of coalescence and SIP in CuCg clouds. In this paper we describe the SPICULE field campaign conducted in 2021, the instrumentation on the two research aircraft and preliminary results from two case studies. The case studies focus on the effects of cloud-base microphysical and state parameters, including temperature, drop size distribution, and total drop concentration, with the development of coalescence and a hypothesized SIP that results from the FFD.

Project logistics, instrumentation, and measurements

The SPICULE project was staged out of Rocky Mountain Metropolitan Airport (KBJC) in Broomfield, Colorado, from 29 May to 25 June 2021. Two research aircraft flew highly coordinated missions to investigate CuCg clouds: 1) a Gulfstream V (GV) owned by the National Science Foundation (NSF) and operated by the National Center for Atmospheric Research (NCAR) Research Aviation Facility (RAF), and 2) a Learjet model 35A operated by SPEC Incorporated of Boulder, Colorado. As shown in Fig. 1 and Table 1, both research aircraft were equipped with a suite of advanced cloud microphysical sensors, air motion systems and airborne cloud radar. The cloud particle probes include the 2D-S (stereo) probe (Lawson et al. 2006); SPEC high volume precipitation spectrometer (HVPS) (Lawson et al. 1998); SPEC fast forward scattering spectrometer probe (FFSSP) and fast cloud droplet probe (FCDP) (O'Connor et al. 2008; Lawson et al. 2017); SPEC Hawkeye combination FCDP, 2D-S (2D10: 10- μm channel; 2D50L: 50- μm channel), and cloud particle imager (CPI) (Lawson et al. 2001; Woods et al. 2018); Droplet Measurement Technologies (DMT) cloud droplet probe (CDP) (Lance 2012); digital holographic particle imager (HOLODEC) (Spuler and Fugal 2011); PMS King liquid water content (LWC) probe (King et al. 1978); Nevzorov LWC and ice water content (IWC) probe (Korolev et al. 1998); and DMT passive cavity aerosol spectrometer probe (PCASP) (Cai et al. 2013). A Ka-band radar viewing up and down at 5 Hz was installed in a standard wing canister on the Learjet. The GV carried a W-band radar that was operator switched from up to down viewing.

In addition, the GV had inlet-based sampling of cloud condensation nuclei (CCN; DMT CCNc) (Roberts and Nenes 2005), biological particles (DMT WIBS-4A) (e.g., Twohy et al. 2016) and INPs via both a continuous flow diffusion chamber (CFDC) and filters collected for offline immersion freezing measurements following resuspension of particles in pure water (e.g., Levin et al. 2019; Barry et al. 2021). The CFDC also sampled residual nuclei from a counterflow virtual impactor (CVI) inlet during GV cloud penetrations to ascertain INPs within cloud (e.g., Levin et al. 2019). The same clean protocols for INP sampling and processing of filter samples were used as are detailed in Barry et al. (2021), including the use of two 47-mm diameter, precleaned in-line aluminum filter holders fitted with precleaned, 0.2- μm pore diameter Nuclepore polycarbonate filter membranes. The same experimental sampling configurations that affect transmission of particles to the CFDC and inline filter collectors that applied in Barry et al. (2021) also apply in this study, such that we determined 50% or higher transmission of particles at sizes below about $\sim 3 \mu\text{m}$, and limited or no sampling of particles larger than 5 μm .

Each aircraft flew 10 research missions that ranged in latitude from south-central Oklahoma to northeast South Dakota (Fig. 2). As seen in Fig. 2, most of the flights produced stacked tracks as the two aircraft coordinated on CuCg cloud systems. The basic flight plan was for the GV to launch prior to the Learjet and make subcloud aerosol/INP measurements. After the GV conducted subcloud measurements the Learjet typically arrived at the target area. Since the Learjet had a maximum 4-h duration and the GV had >8-h duration, when the target area was



Fig. 1. Instruments installed on the (left) Learjet and (right) GV for the SPICULE project. (a) Learjet right wing: AIMMS-20 and FCDP in tip tank, 2D-S and 2D-Gray probes on pylon. Hawkeye installed on bottom of fuselage shown in inset. (b) Learjet left wing: FFSSP in tip tank, KPR radar and HVPS on wing pylon. (c) GV right wing: 2D-C, 2D-S, FCDP, HCR radar, and Hawkeye. (d) GV left wing: CDP, PCASP, HOLODEC, and HVPS [photo credits: Learjet: Code10 Photography; Gulfstream V: Pavel Romashkin; panel (a):Ted Fisher; panel (b):Sarah Woods; panels (c) and (d): Kyle Holden].

more than about 300 n mi (1 n mi = 1.852 km) from KBJC the Learjet would preposition to a nearby airport and refuel. On rare occasions both aircraft would preposition when the target area was distant or timing of the development of CuCg was uncertain. Forecasting was critical so that the subcloud measurements could be made before the CuCg developed into major cloud systems or dissipated all together. The project received excellent forecasting support from Dr. David Lerach at the University of Northern Colorado.

The two aircraft coordinated on a target cloud that was growing and had a cloud-top temperature $\geq -5^{\circ}\text{C}$. The GV would make a pass just below cloud base to measure temperature, pressure, updraft, and aerosol characteristics, and then climb and make a penetration to measure the drop size distribution (DSD) about 300 m above cloud base. The Learjet would typically make its first penetration in the region from 0° to -3°C to measure the DSD and updraft, and determine that the cloud “turret” was free of measurable ice. CuCg clouds are mostly found in clusters, but individual turrets that are growing will often tower above the cloud tops in the cluster. Since downdrafts are typically observed at the edges of an updraft (Heymsfield et al. 1979; Moser and Lasher-Trapp 2017; Blyth et al. 1988; Morrison et al. 2020; L22), it is important to determine that a fresh updraft is not contaminated with ice that has

Table 1. List of instrumentation installed on the Learjet and GV for the SPICULE project.

Learjet		Gulfstream V		
Instrument	Range	Instrument	Range	
Temperature: Rosemount Model 102 and 510BH sig. cond.	-50° to +50°C	Temperature (fast response): Rosemount	-50° to +50°C	
Altitude: RVSM certification	45,000 ft	Temperature (heated): Rosemount	-50° to +50°C	
Airspeed: RVSM certification	0–220 m s ⁻¹	Cloud drops: DMT CDP:	2–50 μm	
Dewpoint temperature: EdgeTech Model C-137	-50° to +50°C	Giant Nuclei Impactor (GNI): NCAR RAF	0.7–16 μm	
Cloud liquid water/total water: SkyPhysTech Nevzorov Probe	0–4 g m ⁻³	2D-C: PMS/DMT	50–1,600 μm	
Ka-band up/down Doppler radar: ProSensing Model KPR	30-m bins	Dewpoint: Buck Research	-60° to +50°C	
Icing detector: Rosemount Model 871LM5	—	Dewpoint (VCSEL): Southwest Sciences	-90° to +30°C	
Aircraft position: AvenTech AIMMS-20	<1 m	Winds: Gulfstream INS	<1 m	
Aircraft heading: Sperry directionalgyro	0°–360°	CVI: NCAR RAF	—	
Winds: AvenTech AIMMS-20	0°–360° 1–100 m s ⁻¹	Cloud nuclei (CN) counter: TSI-3760A	Particles > 11 nm up to 10,000 cm ⁻³	
Cloud particles: SPEC 2D-S	10 μm–3 mm	CCN: DMT	0.1–3 μm	
Cloud particles: SPEC 2D-Gray	10 μm–3 mm	Cloud particles: SPEC 2D-S	10 μm–3 mm	
Cloud drops: SPEC FFSSP	2–50 μm	Cloud drops: SPEC FCDP	2–50 μm	
Precipitation particles: SPEC HVPS-3	150 μm–3 cm	Precipitation particles: SPEC HVPS-3	150 μm–3 cm	
Combination probe for cloud drops, particles, and high-resolution particle images: SPEC Hawkeye	FCDP: 2–50 μm	Combination probe for cloud drops, particles, and high-resolution particle images: SPEC Hawkeye	FCDP: 2–50 μm	
	2D-S: 10 μm–3 mm		2D-S: 10 μm–3 mm	
	50 μm–1 cm		50 μm–1 cm	
	CPI: 5 μm–2 mm		CPI: 5 μm–2 mm	
			Icing detector: Rosemount (Model 871)	—
			LWC: PMS King Probe	0.05–3 g m ⁻³
			Cloud particles: NCAR EOL HOLODEC	23–1,000 μm
			Aerosol particle size: DMT PCASP	0.1–3 μm
			Ice nucleating particles (INP): CSU CFDC; CSU IS	0° to -30°C
			Biological particles: DMT WIBS-4	0.8–20 μm
	W-band radar Doppler (HCR): NCAR EOL	30–150 m		

been transported downward in downdrafts. It is also possible for SLDs to be transported downward in adjacent downdrafts.

After its initial cloud penetration 300 m above cloud base the GV would climb outside of cloud in ~2,000-ft (610 m) increments while the Learjet did likewise, starting its climb after a penetration within the region from 0° to -3°C. The goal was for the GV to climb and make penetrations to document the warm-cloud DSD development while the Learjet documented DSDs and ice particle development above the 0°C level. Both the Learjet and GV had pictorial views of the location and altitude of the other aircraft, with the goal of making simultaneous stacked penetrations of the same cloud. Due to air traffic control (ATC) restrictions this was not always possible, but the two aircraft almost always worked within the same cloud complex. Of particular interest were CuCg that developed a weak-to-moderate collision-coalescence

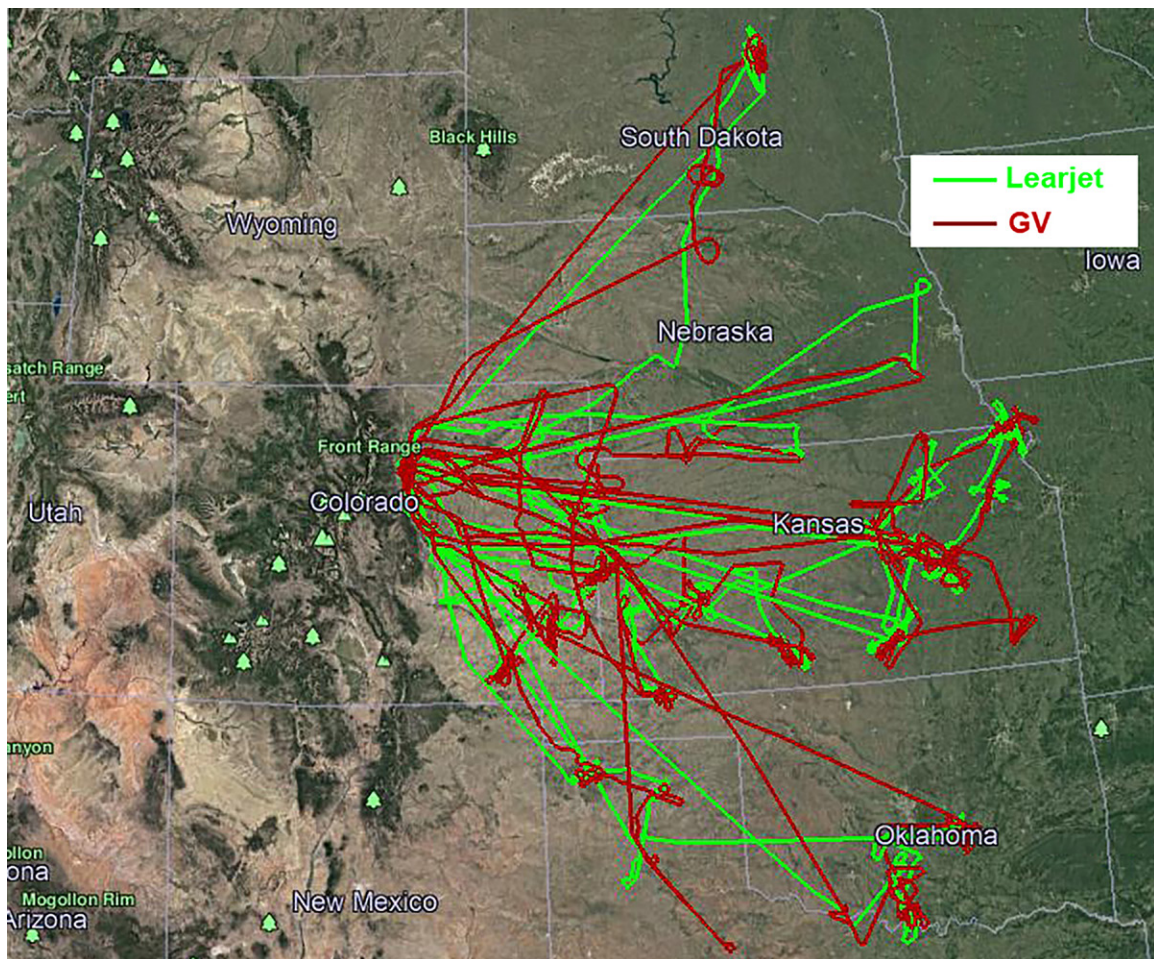


Fig. 2. Flight tracks for the 10 SPICULE missions conducted by the GV and Learjet.

process that may or may not lead to a SIP via the FFD process (Koenig 1963; Lawson et al. 2015, 2017; L22; Phillips et al. 2018). We point out that observations of aircraft-produced ice particles (APIPS) have been observed in association with turbo prop aircraft (Rangno and Hobbs 1983; Heymsfield et al. 2011), but that APIPS have not been documented in association with jet aircraft.

In situ data collected in CuCg from recent investigations have shown that the development and intensity of coalescence and the FFD SIP is linked to cloud-base temperature and the breadth of the cloud-base DSD (Lawson et al. 2017; L22). The product of cloud-base temperature, T_{CB} (K), and the diameter of the maximum drop size, DSD_{max} (mm), measured about 300 m above cloud base is called the convective coalescence potential, ζ , which can be used as a predictor of whether a CuCg will develop a moderate to strong coalescence process and associated FFD SIP, or weak or no coalescence without the FFD SIP (L22). $DSD_{max} \geq 50 \mu\text{m}$ is measured by the 2D-S OAP, which has a sample volume that is a function of the square of drop diameter until the optical depth of field reaches the distance between the sample windows, and is constant thereafter (Lawson et al. 2006). For a $50\text{-}\mu\text{m}$ diameter drop the sample volume for a 10-s cloud sample at 150 m s^{-1} is 49 L, and for drops $\geq 100\text{-}\mu\text{m}$ diameter it is 196 L. A DSD with 100 cm^{-3} total drop concentration has a typical concentration of $50\text{-}\mu\text{m}$ drops of about 1 L^{-1} and a concentration of $100\text{-}\mu\text{m}$ of about 0.1 L^{-1} (Lawson et al. 2015). Thus, in a 10-s cloud pass the 2D-S will size about forty-nine $50\text{-}\mu\text{m}$ drops and twenty $100\text{-}\mu\text{m}$ drops. In addition, the 2D-S $50\text{-}\mu\text{m}$ pixel OAP has 4 times the sample volume of the 2D-S $10\text{-}\mu\text{m}$ channel and will size forty $100\text{-}\mu\text{m}$ diameter drops.

We define the convective coalescence potential as $\zeta = T_{CB} \times DSD_{max}$. L22 show that CuCg in the Caribbean with a T_{CB} of 24°C (297.15 K) and a DSD_{max} of $100 \mu\text{m}$ (0.1 mm) have a

$\zeta = 29.7$ K mm. CuCg with $\zeta > \sim 23$ K mm have been observed to produce strong coalescence and a SIP that appeared to play a major role in converting an all-liquid updraft to almost completely frozen hydrometeors in less than 8 min (e.g., Fig. 2, Lawson et al. 2015). Conversely, CuCg investigated on the High Plains with a T_{CB} of 5°C and a DSD_{max} of $20\ \mu\text{m}$ have a $\zeta = 5.6$ K mm, and do not produce any distinguishable coalescence or FFD SIP. CuCg in an intermediate range with a ζ ranging from about 8 to 17 K mm display weak to moderate coalescence and FFD SIP rates. As shown in Table 2, CuCg sampled during SPICULE research flights had T_{CB} values in the range from -2° to 22°C . Table 2 also shows dates, times, and locations of missions, estimates of cloud-base altitude, cloud-top altitude, cloud-top temperature (T_{CT}), presence of SLDs, and comments that include a bronze, silver, or gold ranking of the missions. A primary objective of the SPICULE field campaign was to investigate CuCg with ζ products in the 8–17 K mm range, and to interpret the relative contributions of T_{CB} , DSD_{max} and the cloud-base drop concentration on the coalescence process and FFD SIP.

Case studies

Overview. The objective of this section is to demonstrate, based on measurements collected during two SPICULE missions, how cloud microphysics/dynamics and aerosol loading may affect the rate of coalescence and FFD SIP. We present data and interpret results from case studies on 5 June 2021 (RF04b) and 11 June 2021 (RF06b). The selected clouds represent two contrasting cases of two seemingly similar CuCg, one in which the ice particle concentration ranged from 588 to $2,351\ \text{L}^{-1}$ in the temperature range from -14° to -17.6°C (RF04b), whereas the second cloud (RF06b) exhibited no ice in this temperature range. Based on the observation of very rapid generation of ice, we hypothesize and show measurements that indicate FFD SIP was most likely responsible for the rapid generation of ice particles in the RF04b case. Data from the two case studies are first discussed in comparison with previous investigations presented in L22, which examines CuCg data collected from five field campaigns in six geographic locations. As explained above, L22 argue that the development and strength of coalescence and the FFD SIP are a strong function of ζ . The two cases investigated here have a T_{CB} of 17.5°C (RF04b) and 22.0°C (RF06b). The RF04b T_{CB} is similar to CuCg T_{CB} 's studied over the southeast United States (SEUS) during the Studies of Emissions, Atmospheric Composition, Clouds and Climate Coupling by Regional Surveys (SEAC⁴RS) project, and the RF06b T_{CB} is very close to the mean T_{CB} of CuCg investigated over the South China and Philippine Seas during the Cloud, Aerosol and Monsoon Processes Philippines Experiment (CAMP²Ex). As will be seen in later sections, the main difference between the SPICULE cases and the CuCg from the other field projects is the very high subcloud aerosol and cloud-base drop concentrations in the SPICULE cases.

It has long been known that a broader cloud-base DSD promotes coalescence in CuCg. Squires (1958) concluded that a cloud-base drop spectrum characterized by relatively low concentration with large average and maximum droplet sizes is favorable for developing coalescence. It has also been suggested that the presence of giant and ultragiant CCN increase DSD_{max} and enhance the coalescence process (Johnson 1982). Morrison et al. (2022) simulated the development of coalescence in a CuCg with a T_{CB} of 10°C , a high ($612\ \text{cm}^{-3}$) subcloud aerosol concentration with ultragiant subcloud aerosols and found a very weak coalescence process. However, when they reduced the subcloud aerosol concentration by a factor of 10 the simulated cloud developed 10 times more millimeter drops at the 0°C level. In this case, the reduction in subcloud aerosol concentration resulted in an order of magnitude decrease in cloud-base drops $< 15\ \mu\text{m}$, and a commensurate increase in drops from 15 to $30\ \mu\text{m}$. Pinsky et al. (2001) show that $60\text{-}\mu\text{m}$ drops have an order of magnitude higher probability of colliding with drops in the 15– $30\text{-}\mu\text{m}$ size range than with drops $< 15\ \mu\text{m}$ in diameter.

Table 2. List of missions flown by the Learjet and GV during SPICULE. CB is cloud base; CT is cloud top. Flight quality rates the missions by bronze, silver, and gold; SLDs indicate the presence of supercooled large drops (order millimeter diameter).

Flight No.	Date	Lear times (UTC)	GV times (UTC)	Location	Estimated CB (kft)	Estimated CB (°C)	Estimated CT (kft)	Estimated CT (°C)	Comments	Flight quality	SLDs
RF01a	29 May 2021	1618–1726	1530–2000	South east Colorado	5.6	—	—	—	Transit and some research	<i>Bronze</i> : Limited research and cold T_{CB}	None
RF01b	29 May 2021	1801–1925		Southeast Colorado	14	–3	20	–18	Some research and transit		
RF02a	1 Jun 2021	1720–1926	1700–2120	East Colorado–west Kansas	8-9	7	22	–24	Transit and research	<i>Silver</i> : Several cloud passes. ATC difficulty	None
RF02b	1 Jun 2021	1959–2112		East Colorado–west Kansas	8	7	—	—	Research and transit		
RF03a	2 Jun 2021	1909–1958	2055–2535	West central and south central Kansas	9	4	13	–3	Transit and a few cloud passes	<i>Bronze</i> : Several cloud passes; T_{CB} out of desired range	None
RF03b	2 Jun 2021	2120–2435		West central and south central Kansas	9	4	20.5	–19	Research and transit		
RF04a	5 Jun 2021	1412–1534	1355–1542	North central Texas–south central Oklahoma	1.8–5	18	>7	10	Transit and a few cloud passes	<i>Gold</i> : Good cloud evolution. Some ATC difficulty.	Yes
RF04b	5 Jun 2021	1738–2056	1743–2210	North central Texas–south central Oklahoma	5; 3.5	13; 17	22	–18	Research		
RF05a	9 Jun 2021	1757–1838	2000–2340	East central South Dakota	6.4	16.5	11	10	Transit and a few cloud passes	<i>Gold</i> : Several good cloud passes. Strong updrafts. Bubbles that eroded bases.	Yes (few)
RF05b	9 Jun 2021	2031–2326		East central South Dakota	8	14	22.5	–18	Research and transit		
RF06a	11 Jun 2021	1556–1703	1805–2415	East Kansas	4.5	20	7.5	20	Transit and a few cloud passes	<i>Gold</i> : Several good cloud passes, strong updrafts	Yes
RF06b	11 Jun 2021	1912–2112		East Kansas–west Missouri	4	22	22	–17	Research		
RF06c	11 Jun 2021	2154–2418		East Kansas	4.5	20	23	–18	Research and transit		
RF07b	17 Jun 2021	2210–2415	2157–2443	South central Nebraska–north central Kansas	16.5	–2	23	–19	Research and transit	<i>Bronze</i> : Not much workable cloud	
RF08b	20 Jun 2021	2117–2409	2126–2621	Northeast Kansas–northwest Missouri	9; 6; 8.5	15; 21; 13	23	–16	Research	<i>Gold</i> : Several good cloud passes near large storm	None
RF08c	20 Jun 2021	2446–2701	2704–2810	Northeast Kansas–northwest Missouri	9.5; 8	12; 17	23	–15	Research and transit		
RF09a	24 Jun 2021	1830–1929	2025–2345	Southwest Kansas	6.5	18	20; 8	–12; 17	Transit and a few cloud passes	<i>Silver</i> : Some good cloud passes in weak turrets, clear air ice	None
RF09b	24 Jun 2021	2027–2322	2025–2345	Southwest Kansas	7.5; 13.8	18; 3	20		Research and transit		
RF10b	25 Jun 2021	2035–2228	1903–2245	North Texas–south Oklahoma	9.5; 11	13.5; 12	23		Research	<i>Silver</i> : Strong updrafts	None

RF04b (5 June 2021). The GV and Learjet conducted a coordinated study of CuCg over the vicinity of the Canadian River just north of Ada, Oklahoma. Figure 3a shows the portion of the flight tracks when both aircraft were penetrating a system of CuCg, and Fig. 3b shows the Springfield, Oklahoma (SGF), 0000 UTC 6 June 2021 sounding. The measured cloud-base temperature of 17.5°C corresponds to a pressure of 890 mb (1 mb = 1 hPa) and altitude of 1,180 m (3,870 ft). The sounding in Fig. 3b indicates a weak convective available potential energy (CAPE) of 202 J kg⁻¹. The 1200 UTC 5 June 2021 sounding showed a strong inversion between 750 and 700 mb that had to be overcome in order for the CuCg to grow to higher altitudes observed by the Learjet. Tables 3 and 4 list microphysical parameters measured in updraft cores by the GV and Learjet during cloud penetrations between 1944 and 2034 UTC.

The Learjet drop concentrations data in Table 4 are measured using an FFSSP, which was also used in the other Learjet campaigns referenced here (Lawson et al. 2015, 2017; L22). An FCDP was also installed on the Learjet for SPICULE and the other campaigns. Compared with the FFSSP, the FCDP generally (but not always) read higher counts in the smallest size bins, especially in regions with high drop concentrations. It is not possible to determine if the FFSSP is not detecting some of the smallest droplets, or whether the FCDP is falsely registering droplets in the smallest channels. The GV did not fly an FFSSP, and instead, an FCDP and a CDP were installed. We have included droplet concentrations from both the FCDP and CDP in Table 3. On the average, total drop concentration between the FCDP and CDP agreed to within about 10%, but 1-Hz values occasionally differed by as much as 50%. In general, the FCDP appears to see more droplets in the smallest bins when concentrations are very high (i.e., >~1,200 cm⁻³), and the CDP reads higher values when the drop concentrations are relatively lower and the DSD is broader. We do not offer an explanation, and instead present the data for the reader to consider and evaluate. We show the GV FCDP and Learjet FFSSP measurements in figures in this paper.

Average subcloud aerosol concentrations measured on this day were variable, with PCASP ranging from about 100 to 1,000 cm⁻³ and CN from 500 to 5,000 cm⁻³. For this study we have chosen average aerosol concentrations immediately below bases of the clouds studied. The average PCASP aerosol concentration measured by the GV immediately below cloud base from

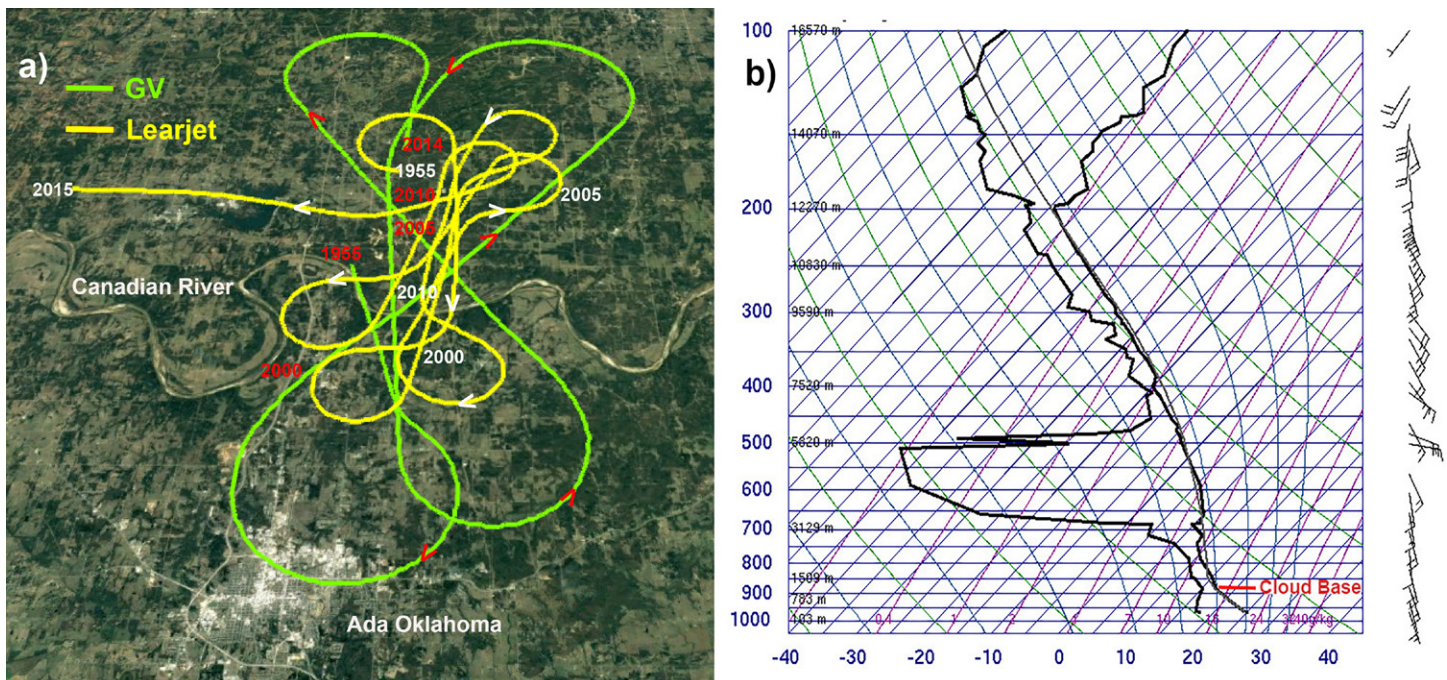


Fig. 3. (a) Portion of GV and Learjet flight tracks relevant to RF04b case study; (b) Springfield (SGF) 0000 UTC 6 Jun 2021 sounding that has a CAPE of 202 J kg⁻¹.

Table 3. List of penetrations of updraft cores by the GV relevant to the RF04b and RF06b case studies. VaV is vertical air velocity; conc. is concentration; LWC is liquid water content; IWC is ice water content; R is derived radar reflectivity; R_{eff} is drop effective radius. LWC and IWC are computed by integrating combined size distributions from all cloud probes.

Date	Time (UTC)	T ($^{\circ}\text{C}$)	VaV _{max} (m s^{-1})	FCDP drop conc. (cm^{-3})	CDP drop conc. (cm^{-3})	FCDP LWC (g m^{-3})	CDP LWC (g m^{-3})	FCDP R (dBZ)	CDP R (dBZ)	FCDP R_{eff} (mm)	CDP R_{eff} (mm)	Ice conc. (L^{-1})	IWC (g m^{-3})
RF04b													
5 Jun 2021	2045:38–2045:41	16.6	1.6	1067	1,016	0.2	0.2	−41.0	−40.0	4.1	4.4	0.0	0.0
5 Jun 2021	2045:55–2045:58	16.5	1.5	1469	1,167	0.3	0.2	−40.1	−40.4	4.1	4.2	0.0	0.0
5 Jun 2021	1944:11–1944:18	16.4	2.1	922	900	0.2	0.2	−39.6	−38.9	4.4	4.6	0.0	0.0
5 Jun 2021	2005:36–2005:42	15.0	2.8	790	753	0.3	0.3	−36.1	−35.1	5.1	5.5	0.0	0.0
5 Jun 2021	2004:58–2005:04	13.0	3.0	756	909	0.5	0.7	−30.6	−28.5	6.5	7.0	0.0	0.0
5 Jun 2021	1954:08–1954:16	8.8	2.8	267	815	0.9	1.6	−21.7	−20.2	10.9	9.9	0.0	0.0
5 Jun 2021	1959:48–1959:54	6.6	3.6	276	448	0.6	1.0	24.4	24.4	11.6	10.9	0.0	0.0
5 Jun 2021	2024:50–2024:55	−1.8	3.4	89	178	1.9	2.4	24.2	24.2	21.4	19.0	0.0	0.0
5 Jun 2021	2025:14–2025:18	−2.0	2.9	192	497	3.1	3.9	23.4	23.4	18.2	16.5	0.0	0.0
5 Jun 2021	2034:04–2034:07	−6.0	5.5	49	90	2.8	3.1	35.6	35.6	41.0	34.6	0.0	0.0
RF06b													
11 Jun 2021	2213:49–2213:53	19.7	1.5	1,157	988	0.4	0.3	−34.8	−34.8	5.0	5.3	0.0	0.0
11 Jun 2021	2215:26–2215:29	19.4	2.0	1,348	1,033	0.4	0.3	−35.1	−36.2	4.9	5.1	0.0	0.0
11 Jun 2021	2145:07–2145:11	15.2	5.6	784	1,022	0.6	0.7	−26.5	−26.9	7.9	7.3	0.0	0.0
11 Jun 2021	2138:17–2138:24	15.1	6.2	816	1,242	0.8	0.9	−25.3	−25.6	7.9	7.3	0.0	0.0
11 Jun 2021	2142:10–2142:16	14.7	4.2	654	796	0.3	0.4	−29.7	−30.0	6.5	6.5	0.0	0.0
11 Jun 2021	2128:13–2128:26	13.5	5.8	701	1,046	0.9	1.0	−22.1	−22.2	9.2	8.3	0.0	0.0
11 Jun 2021	2229:57–2230:01	11.8	5.2	384	820	1.1	1.5	−17.9	−17.7	12.0	10.4	0.0	0.0
11 Jun 2021	2228:53–2228:57	11.3	2.7	385	803	0.4	0.7	−24.5	−23.7	9.2	8.4	0.0	0.0
11 Jun 2021	2150:14–2150:17	11.2	7.5	787	1,098	0.9	1.3	−19.3	−19.1	9.8	9.4	0.0	0.0
11 Jun 2021	2229:39–2229:41	11.1	2.0	810	720	0.5	0.5	−23.9	−23.7	7.7	8.4	0.0	0.0
11 Jun 2021	2229:37–2229:41	10.7	2.8	921	830	0.4	0.5	−25.6	−25.5	6.8	7.6	0.0	0.0
11 Jun 2021	2151:47–2151:51	9.9	4.8	418	837	0.9	1.3	−20.1	−19.5	10.6	9.8	0.0	0.0

2010:00 to 2010:20 UTC was 520 cm^{-3} , and the average CN concentration was $1,676 \text{ cm}^{-3}$. As shown in Fig. 4a, the average drop concentration measured 300 m above cloud base by the FCDP on the GV was 922 cm^{-3} . The CDP measured 903 cm^{-3} over the same time period.

Table 4. As in Table 3, but for the Learjet.

Date	Time (UTC)	T (°C)	VaVmax (m s ⁻¹)	Drop conc. (cm ⁻³)	LWC (g m ⁻³)	R (dBZ)	R_{eff} (μm)	Ice conc. (L ⁻¹)	IWC (g m ⁻³)
RF04b									
5 Jun 2021	1954:15–1954:21	–2	6.6	400	3.0	–4.8	15.8	0	0.0
5 Jun 2021	1958:00–1958:07	–5.8	3.7	142	2.9	25.6	22.1	0	0.0
5 Jun 2021	2004:00–2004:04	–8.5	9.2	117	2.3	23.8	20.3	0	0.0
5 Jun 2021	2006:29–2006:32	–10.5	5.6	126	3.5	29.6	25.7	0	0.0
5 Jun 2021	2008:44–2008:46	–14	8.1	87	2.4	32.9	45.0	30	0.3
5 Jun 2021	2011:19–2011:21	–16.5	5.3	40	0.4	36.5	64.0	2,351	1.0
5 Jun 2021	2013:05–2013:08	–17.6	2.9	16	0.1	29.6	60.0	588	0.7
RF06b									
11 Jun 2021	2210:09–2210:13	–0.9	10.4	547	2.2	–15.4	11.6	0	0.0
11 Jun 2021	2207:08–2207:11	–1.2	8.6	419	1.4	0.8	10.8	0	0.0
11 Jun 2021	2232:12–2232:15	–4	12.2	735	3.9	2.3	13.8	0	0.0
11 Jun 2021	2215:10–2215:14	–5.5	8.3	336	2.1	21.6	15.6	0	0.0
11 Jun 2021	2234:34–2234:37	–10.9	7.9	687	1.9	10.7	12.9	0	0.0
11 Jun 2021	2218:08–2218:12	–11	4.7	399	1.7	22.8	17.4	0	0.0
11 Jun 2021	2236:22–2236:26	–13.7	7.7	287	1.2	7.5	16.2	0	0.0
11 Jun 2021	2240:14–2240:17	–14.3	13.6	313	1.2	2.3	14.9	0	0.0
11 Jun 2021	2226:48–2226:58	–17.8	23.1	438	2.3	21.2	14.5	0.02	0.001

The cloud-base drop concentration was higher than the PCASP subcloud measurement and lower than the CN value, implying that a portion of the CCN came from aerosols smaller than 0.1 μm. The CCN counter was inoperative during this time period.

Figure 4 shows cloud-base DSDs from RF04b and SEAC⁴RS over the SEUS (Fig. 4a) compared with (Fig. 4b) RF04b and SEAC⁴RS in ice-free updraft cores aloft. Figures 4c and 4d show comparisons in a similar format from RF06b and CAMP²Ex. Figure 4a shows that the mean cloud-base drop concentration measured during SEAC⁴RS (628 cm⁻³) was about 70% of the RF04b value. What is apparent in the comparison of DSDs in Fig. 4a is the much higher concentrations of drops in the 2–10 μm size range in RF04b compared with the mean DSD from SEAC⁴RS. In addition, the SEAC⁴RS cloud-base DSDs extend out to much larger values of DSD_{max} (65 compared with 30 μm for RF04b). Thus, the RF04b ζ is 290.5 K × 0.030 mm = 8.7 K mm compared with 291 K × 0.065 mm = 18.9 K mm for SEAC⁴RS. Based on the discussion above and Table 2 in L22, the RF04b ζ suggests weak coalescence compared with moderate coalescence in SEAC⁴RS.

Figure 4b shows a comparison of RF04b and SEAC⁴RS DSDs in moderate-to-strong (i.e., ~5–20 m s⁻¹) updrafts in ice-free cloud. The DSDs in Figs. 4a and 4b show that a stronger coalescence process did develop in SEAC⁴RS CuCg. This may be attributed to the larger SEAC⁴RS DSD_{max} coupled with a lower concentration of drops < 10 μm and a higher concentration of drops > 10 μm. Thus, even though the SEAC⁴RS and RF04b T_{CB} values were nearly identical, the smaller concentration of drops < 10 μm and larger DSD_{max} appear to have a significant impact on the development of coalescence aloft in the SEAC⁴RS CuCg.

A more detailed discussion of the case study of RF06b is presented later in the “RF06b (11 June 2021)” section. However, for the sake of consistency, we present RF06b and CAMP²Ex DSDs for cloud base and aloft in ice-free cores in Fig. 4. Figure 4c shows the mean cloud-base DSD from CAMP²Ex measured over the Philippine and South China Seas compared with the cloud-base DSD measured by the GV from 2215:26 to 2215:29 UTC. Figure 4c shows a much higher total concentration of drops (1,348 cm⁻³) at cloud base for the RF06b case compared

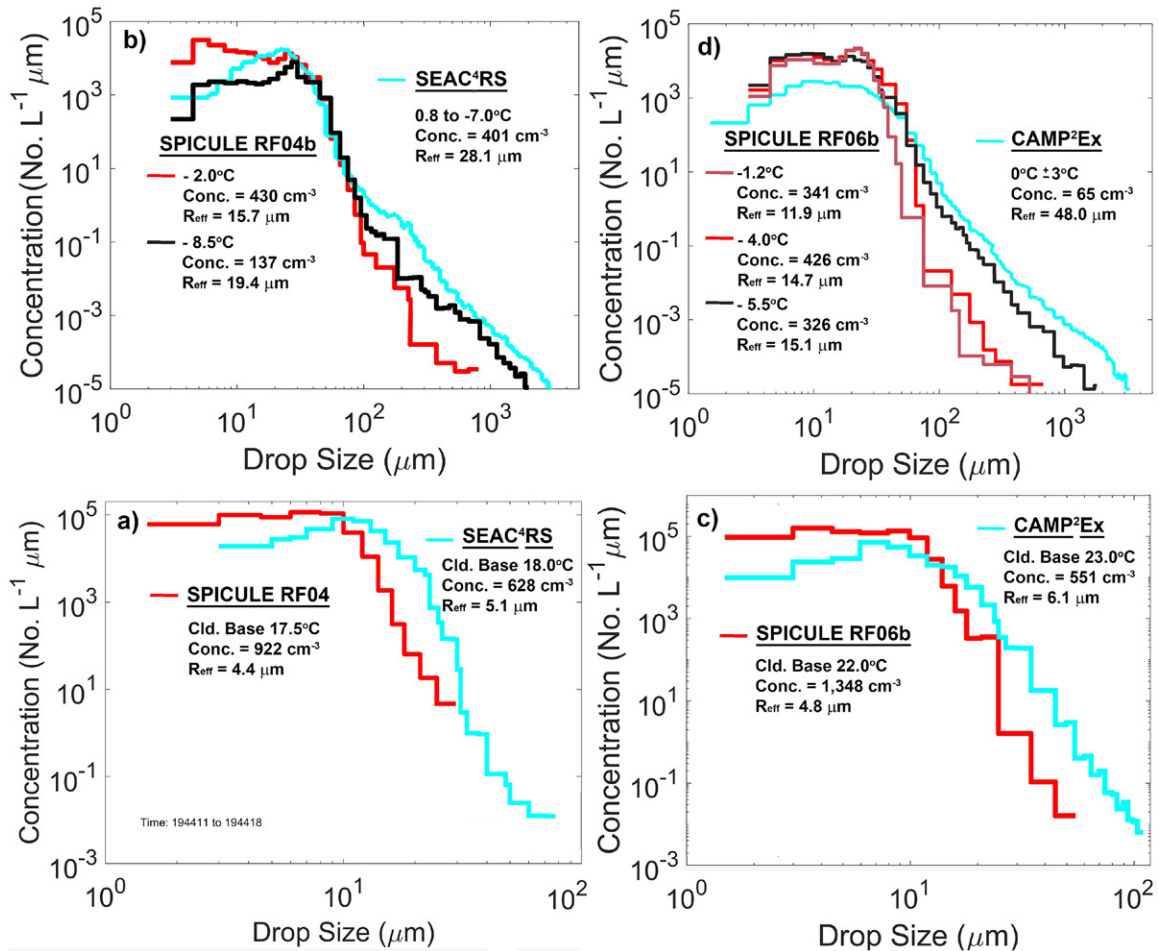


Fig. 4. Comparisons of (a) cloud-base DSDs from RF04b and mean DSD from the SEAC⁴RS project in SEUS; (b) RF04b and SEAC⁴RS DSDs aloft in ice-free updraft cores. (c) Comparison of cloud-base DSDs for RF06b and CAMP²Ex, and (d) DSDs for RF06b and CAMP²Ex aloft in ice-free cores.

with the average from CAMP²Ex cloud-base penetrations (551 cm^{-3}). The RF06b case has a much larger concentration of drops in the 2–15- μm size range compared with the mean DSD from CAMP²Ex. In addition, the CAMP²Ex cloud-base DSD extends to a DSD_{max} of 100 μm compared with 50 μm for the RF06b case. Thus, the RF06b ζ is $295 \text{ K} \times 0.050 \text{ mm} = 14.8 \text{ K mm}$ compared with $\zeta = 296 \text{ K} \times 0.100 \text{ mm} = 29.6 \text{ K mm}$ for CAMP²Ex. Based on the discussion above and Table 2 in L22, the RF06b ζ suggests weak-to-moderate coalescence compared with strong coalescence in the CAMP²Ex studies.

Figure 4d shows a comparison of RF06b and CAMP²Ex DSDs in moderate-to-strong (i.e., $\sim 5\text{--}20 \text{ m s}^{-1}$) updrafts in ice-free cloud. As seen in Fig. 4d, the concentration of large drops above the 0°C level is one to two orders of magnitude higher in the CAMP²Ex clouds than in the RF06b case. The DSDs in Figs. 4c and 4d show that a much stronger coalescence process developed in CAMP²Ex CuCg when the cloud-base DSD contained fewer drops $< 15 \mu\text{m}$ and a higher concentration of drops $> 15 \mu\text{m}$, even though the T_{CB} values were similar. A relatively smaller concentration of drops $< 15 \mu\text{m}$ and a larger DSD_{max} appear to have promoted a stronger development of coalescence aloft in CAMP²Ex CuCg compared with the RF04b case.

L22 show a plot (their Fig. 15) from several geographic locations of ζ versus the elevation in CuCg where the LWC decreases to about 10% of the adiabatic LWC. As generally described above, the L22 data show a trend where clouds with relatively low ζ values do not produce coalescence and a SIP, with an exponentially increasing amount of coalescence and SIP aloft (i.e., decrease in LWC) as ζ increases. While the trend in L22 appears to be robust, additional studies, and particularly numerical simulations with advanced bin microphysics (e.g., Morrison et al. 2022),

should be able to improve our understanding of the contribution of small (<~15 μm) drops.

Both simulations and observations show that a value of cloud drop effective radius (R_{eff}) from about 12 to 14 μm is associated with an active coalescence process in cumulus updrafts (Rosenfeld and Gutman 1994; Gerber 1996; Andreae et al. 2004; Freud and Rosenfeld 2012; Morrison et al. 2022; L22). Figure 5 shows a plot of temperature versus R_{eff} in ice-free updraft cores from various geographic locations, including the RF04b case, with average cloud-base drop concentrations for each location. The gray shaded region in Fig. 5 indicates the (12–14 μm) threshold range of R_{eff} where coalescence is active, based

on literature cited above. The plots in Fig. 5 suggest that both T_{CB} and drop concentration (i.e., subcloud aerosol loading) have an influence on the development of coalescence (i.e., R_{eff}) in CuCg updraft cores. For example, CuCg in the UAE with $T_{\text{CB}} = 10^\circ\text{C}$ barely reached the threshold R_{eff} by the -12°C level, whereas on the other extreme CuCg over the South China and Philippine Seas (CAMP²EX) and Caribbean (ICE-T) with $T_{\text{CB}} = 23^\circ\text{C}$ reached the threshold R_{eff} at 15° to 18°C and produced much stronger coalescence (Lawson et al. 2015; L22). Note that the plot of R_{eff} for ICE-T follows the same pattern as for CAMP²EX, but at a temperature that is about 3°C warmer. The noticeable difference in cloud-base drop concentration, 89 cm^{-3} (ICE-T) versus 579 cm^{-3} (CAMP²EX) strongly suggests that aerosol loading is a factor. The T versus R_{eff} plots for the other geographic locations follow an intermediate pattern between the two (UAE and Caribbean) extremes.

The Learjet started sampling turrets at 1954 UTC at -2°C and continued to climb and penetrate turrets near their tops, making its last penetration at -17.6°C . Figure 6 shows a time series of data from the KPR radar, cloud photos from the Learjet forward-looking video camera, and representative particle images collected on cloud passes. The radar data and visual record in Fig. 6 show that the Learjet penetrated within about 1,000 ft (300 m) of the cloud tops and that there were no higher clouds in the immediate vicinity. The KPR radar profile shows that reflectivity in the centers of the turrets increased with altitude and ascended with cloud tops from 1954 UTC (5,200 m) to 2011 UTC (7,100 m). The maximum reflectivity of the KPR within this time frame reached up to 38 dBZ. Following Matrosov et al. (2005) such high reflectivity in the Ka band is typically associated with rain drops or hail, and snow alone usually does not produce this magnitude of reflectivity. This is consistent with the in situ measurements, which showed that the high reflectivity regions in the center of the turrets contained large water drops in sustained updraft cores. The particle images shown below the radar time series are from the Learjet 2D10 and 2D50 (μm) OAP probes, and high-resolution images from the CPI. The images and radar data support the picture of increasing coalescence with height until the first ice particles (i.e., “first ice”) are detected at -14.0°C .

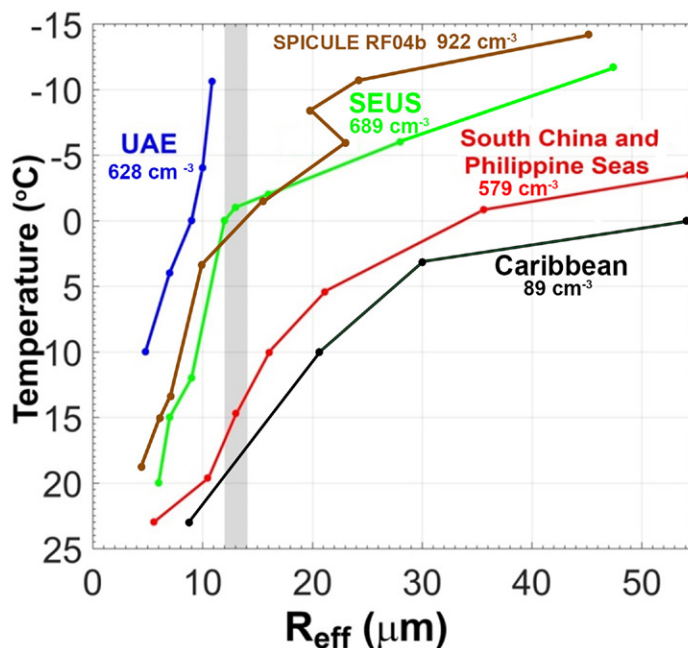


Fig. 5. Plots of temperature vs R_{eff} with average cloud-base drop concentrations for UAE, SEAC⁴RS (SEUS), CAMP²Ex (South China and Philippine Seas), Caribbean (ICE-T), and RF04b case study. The gray shaded region indicates the range of R_{eff} where coalescence is active, based on literature cited in the text.

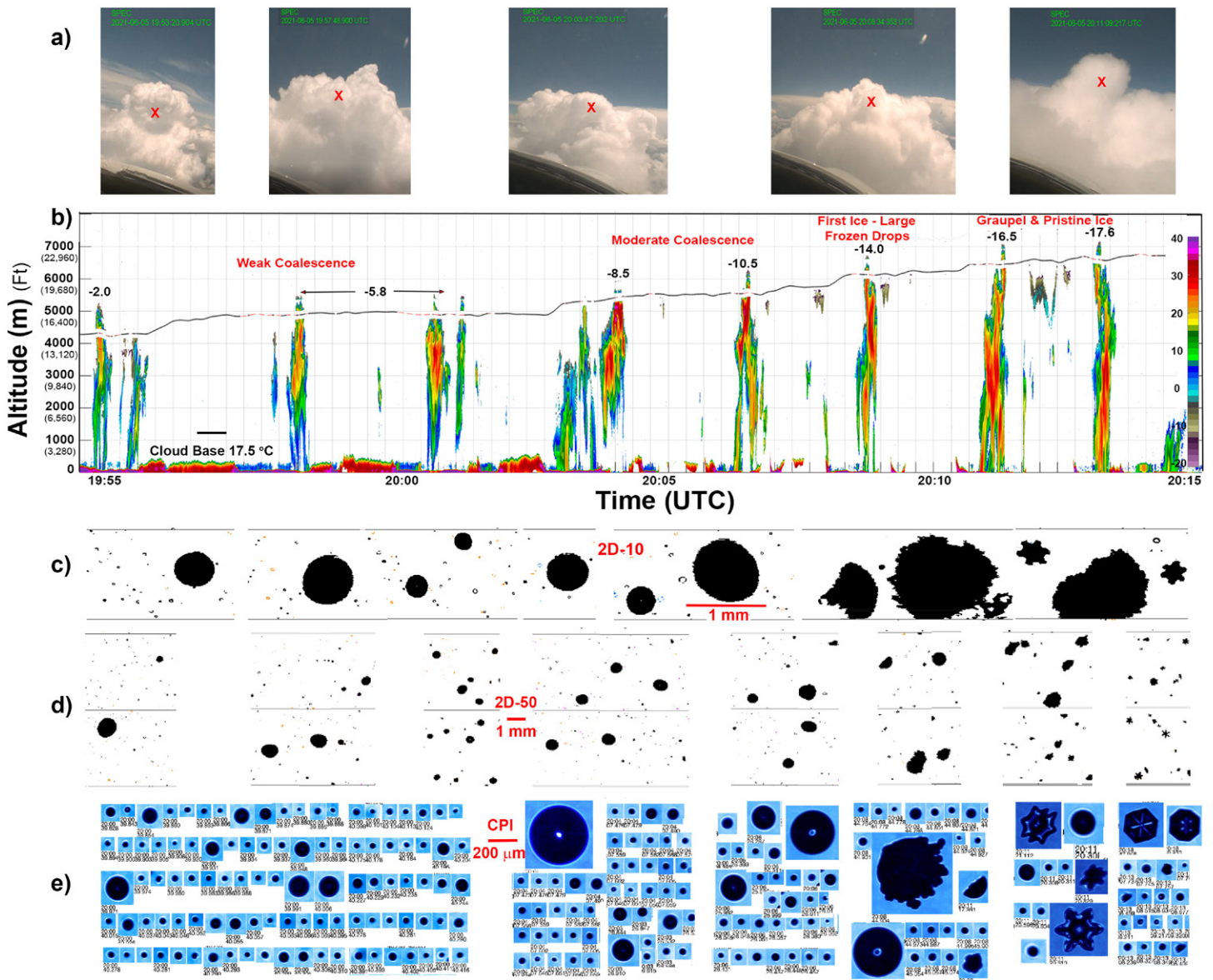


Fig. 6. RF04b measurements showing (a) photos of Learjet flight altitude (black line) penetrations near cloud top (red X), (b) reflectivity measurements from the KPR radar, and examples of particle images from the (c) 2D10, (d) 2D50, and (e) CPI probes.

The first detectable ice that appears during the cloud penetration at -14.0°C (2008:45 UTC) was 150 s later than the ice-free updraft core penetrated at -10.5°C (2006:30 UTC). Thus, the first detectable ice could have formed at any temperature between -10.5° and -14.0°C . From the CPI images, it appears that the first “detectable” ice particles were large frozen SLDs. The CPI does not run continuously like the OAPs, and instead takes discrete snapshots of particles that trigger the probe at a maximum rate of 400 Hz. Thus, the effective sample volume of the CPI is relatively small, on the order of $150\text{ cm}^{-3}\text{ s}^{-1}$ at 150 m s^{-1} . Also, since the probe only takes a snapshot when it is triggered by a particle, in fresh updraft cores of mixed-phase cloud the CPI is dominated by small cloud droplets that occur in orders of magnitude higher concentrations than small ice particles. The bottom line is that the probability of imaging pristine ice in mixed-phase regions is orders of magnitude lower than that for small cloud droplets.

This fact makes comparison to INP concentrations and ascertaining consistency with the predicted onset for primary nucleation of ice difficult. Figure 7 shows that INP concentrations in subcloud regions during RF04b became measurable colder than -14°C in concentrations

somewhat higher than the values predicted by the historical INP measurement parameterization of Fletcher (1962). We also show data from RF06b, where a discrepancy is noted between the online and offline INP measurements. This discrepancy is at the upper bound of ones noted in prior comparisons of immersion freezing measurements made on atmospheric aerosols (DeMott et al. 2017), but it is also the case in aircraft measurements of this type that perfect alignment of the integrated filter sample and higher-frequency CFDC data periods and locations is difficult to achieve within flight constraints while assessing aerosols in the boundary layer around developing storms. We believe this was the issue for that flight. Nevertheless, the data in RF04b and RF06b generally bracket the range of boundary layer INP concentration temperature spectra found during SPICULE, as will be reported in a future publication. Thus, INPs were measurable in RF04b below about -14°C in a range somewhat higher than the values predicted by the early historical INP measurement parameterization of Fletcher (1962). While significant variations of

INP concentrations were observed within single flights and over many flights, a semiexponential INP concentration temperature spectrum was often present, suggesting limited INPs at or below 10^{-2} L^{-1} at $>-10^{\circ}\text{C}$ in most cases. INP concentrations exceeded 0.1 L^{-1} at around -15°C and 1 L^{-1} at around -18°C in RF04b, consistent with an inability to explain cloud ice concentrations through primary nucleation alone.

Once first ice is formed in updraft cores of CuCg, numerous SLDs resulting from a strong coalescence process ignite the FFD SIP. A high concentration of SLDs provides a rapid enhancement of the concentration of ice particles through a chain reaction of freezing of SLDs by secondary ice particles, which then generate subsequent ice particles during fragmentation of freezing SLDs. Freezing of liquid droplets by secondary ice particles along with the Wegener–Bergeron–Findeisen process results in a rapid glaciation process. This sequence is supported by previous observations (Lawson et al. 2015, 2017; L22). Subsequent to the appearance of graupel particles at -14.0°C radar reflectivity in the turrets investigated at -16.5°C (2011:20 UTC) and -17.6°C (2013:05 UTC) indicate that large frozen drops are being transported downward.

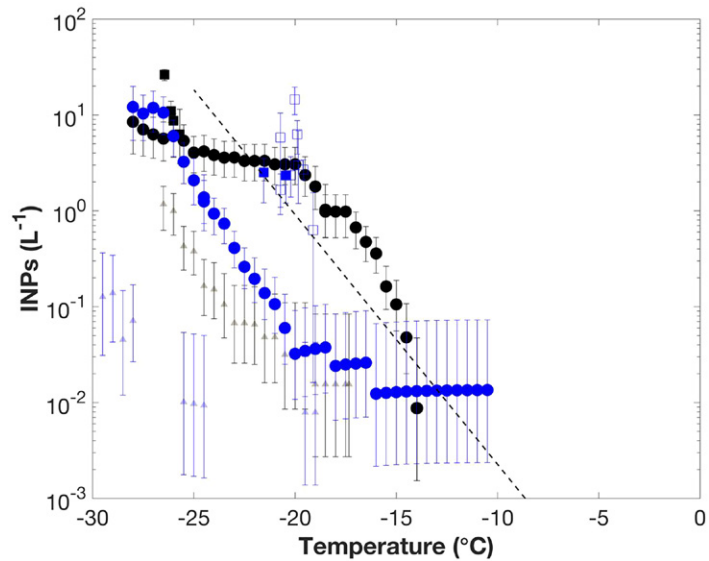


Fig. 7. GV ice nucleating particle (INP) concentration data per standard liter from RF04b (black points) and RF06b (blue points) subcloud regions, measured on the basis of particle suspensions from integrated filter collections tested for immersion freezing (circles) and for integrated few-minute periods by the CFDC instrument (squares), operated to process particles sampled at 1.5 L min^{-1} at well above water saturation at one temperature at a time to emphasize immersion freezing. Filled CFDC data points represent measurements from the isokinetic ambient aerosol inlet, while open points represent reprocessed cloud particle residual INPs, corrected for CVI enhancement factor and the lower cut size of captured droplets. CFDC data are those significant at the 90% confidence interval after background correction as described in Barry et al. (2021). IS data have been corrected by average background INPs per filter from 7 blanks (nonsampled filters) during SPICULE, normalized in each case by the volume collected in the sampled filter. Volume-normalized specific blank filters temporarily exposed to the air but not sampled in RF04b (560 L) and RF06b (320 L) are shown by shaded data points at lower values. Confidence intervals are defined the same for these as for sampled filters. The dashed line represents the average INP concentrations from Fletcher (1962).

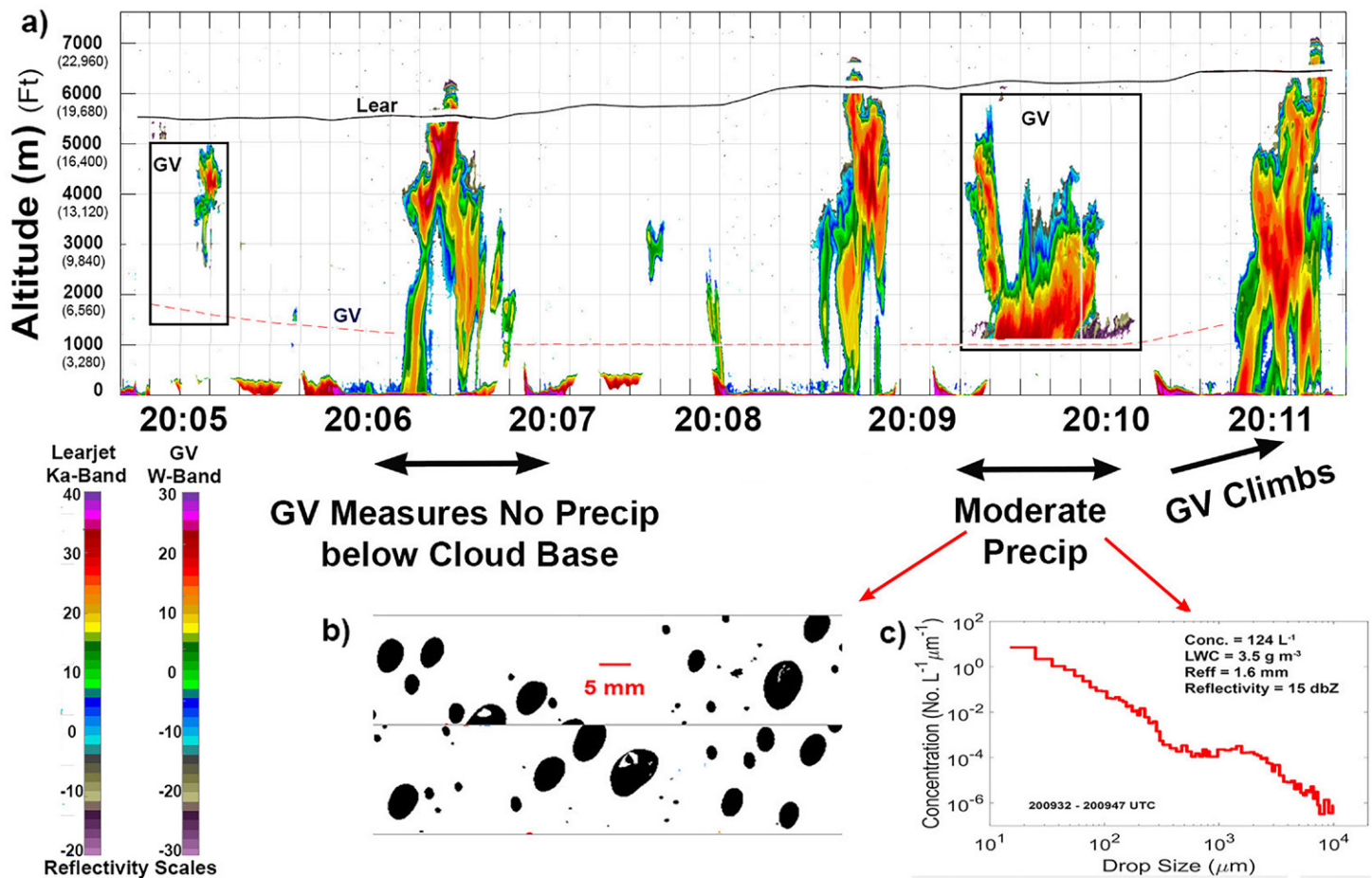


Fig. 8. (a) Reflectivity measurements from the KPR on the Learjet and WCR on the GV (inset boxes) for the RF04b time period 2005–1200 UTC, (b) examples of raindrops observed below cloud base by the GV, and (c) DSD from the raindrop images.

This is supported by the measurements shown in Fig. 8, where GV upward-looking radar reflectivity is inserted into the Fig. 6 time series from 2004 to 2011 UTC. After encountering no precipitation on a subcloud pass at 2006:30 UTC, the GV encountered moderate precipitation below cloud base from 2009:32 to 2009:47 UTC. Figure 8 shows strong W-band reflectivity values at the altitude of the GV and HVPS images of raindrops.

The evolution of coalescence and the effect of rapid freezing of the largest drops are illustrated in Fig. 9, which shows the progression of particle size distributions (PSDs) with decreasing temperature in updraft cores. The progression of an increasing concentration and size of the large drops with a commensurate decrease in concentration of small drops is evident from cloud base to the -17.6°C level. The most likely explanation for this is that the growth of larger drops is at the expense of smaller drops due

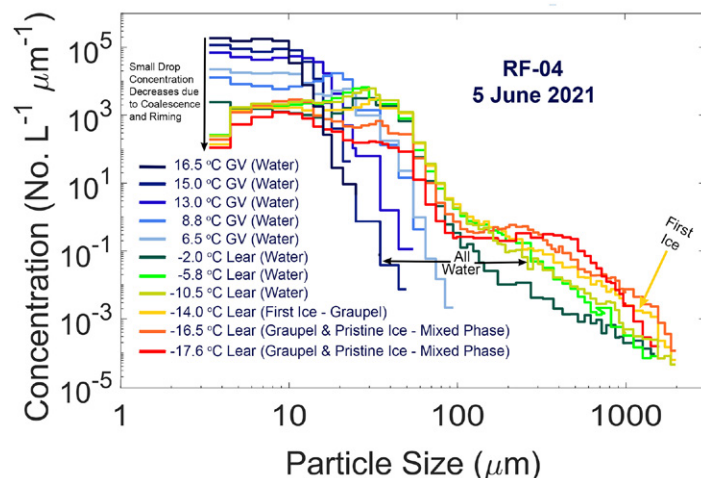


Fig. 9. Color-coded DSDs measured by the GV and Learjet during penetrations of ice-free (water) and mixed-phase updraft cores during RF04b. The “first ice” DSD is shown at -14.0°C .

to an active coalescence process and riming once ice has formed.

Figure 10 shows PSDs separated into water and ice at -14.0° (first ice), -16.7° , and -17.6°C using a combination of automatic and manual classification of the roundness of CPI and OAP particle images. The first ice particles were observed between -10.5° and -14.0°C (Fig. 10a) in a concentration of about 30 L^{-1} , which is already about three orders of magnitude higher than predicted from primary nucleation. This highlights the difficulty in detecting the first ice with cloud penetrations separated by minutes, and also to the high rate of productivity of the hypothesized FFD SIP. The high ice particle concentration and IWC increased rapidly (Fig. 10b) commensurate with a decrease of LWC and an increase in the rate of FFD SIP (L22). The increase in IWC at -16.5° and -17.6°C is mostly associated with millimeter-diameter graupel with some $100\text{--}300\text{ }\mu\text{m}$ pristine stellar dendrites and hexagonal plates (Fig. 6). The modest decrease in ice concentration and IWC from -16.5° (Fig. 10b) to -17.6°C (Fig. 10c) can be primarily attributed to dilution from entrained environmental air, and reduction of the rate of secondary ice production because the rapid freezing of SLDs decreases their concentration. The first ice formed between the cloud penetrations at 2006:32 and 2008:45 UTC, and the 1–2-mm graupel particles are detected at 2011:20 UTC. There is no evidence of heavily rimed ice crystals in the images, so the most likely mechanism of graupel formation is freezing of SLDs.

The images in Fig. 6 also show pieces of fragmented frozen SLDs, which is further evidence that the FFD SIP mechanism is responsible for rapid glaciation (Lawson et al. 2015, 2017; L22). The pristine $100\text{--}300\text{-}\mu\text{m}$ stellar and hexagonal plate ice crystals observed at 2011:20

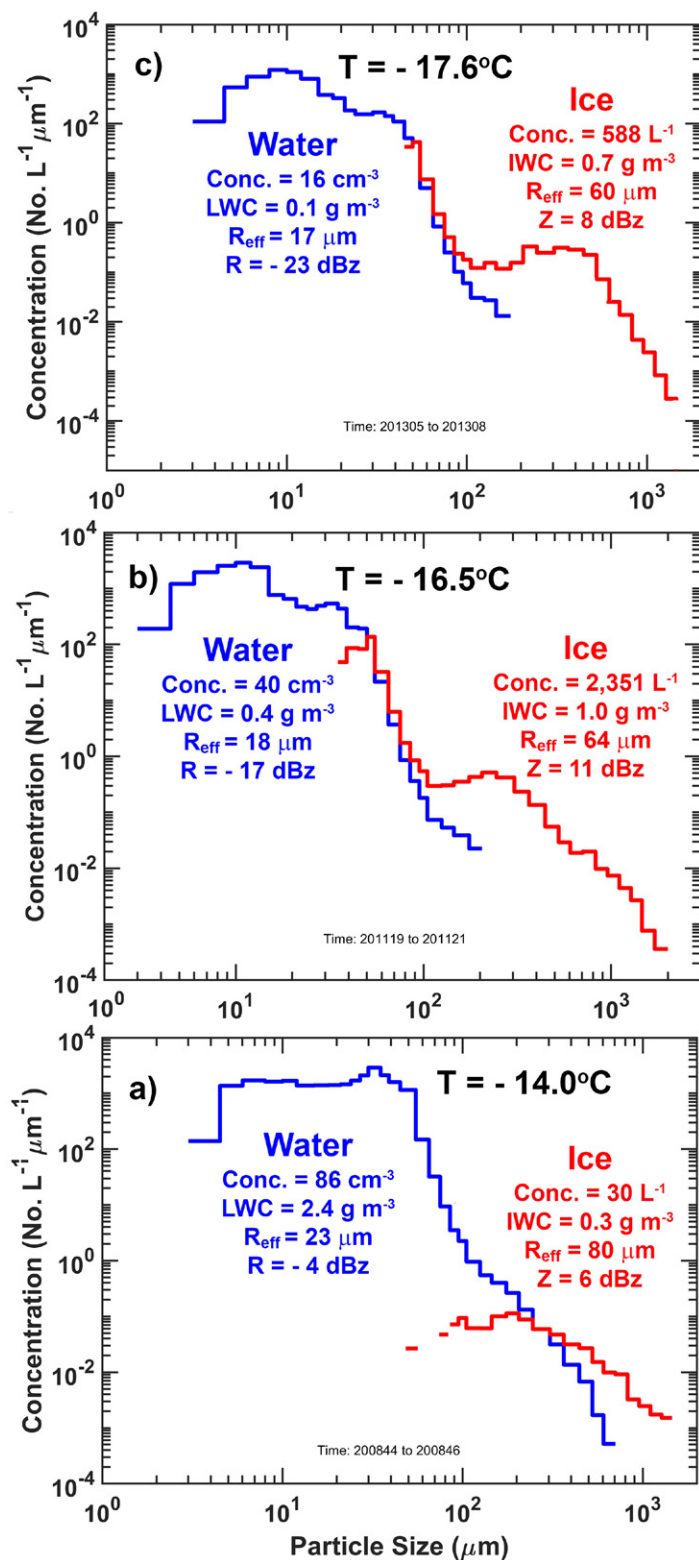


Fig. 10. Water (blue) and ice (red) PSDs separated using particle imagery and shown with bulk properties measured during Learjet cloud penetrations of updraft cores at temperatures shown.

UTC (-16.5°C) and 2013:03 UTC (-17.6°C) are most likely formed on monocrystalline ice particles resulting from FFD SIP (Korolev et al. 2020), or from primary nucleation of frozen droplets, as discussed above. The stellar habit growth is relevant to the temperature range from -12° to -18°C (e.g., Pruppacher and Klett 1997). Therefore, the lowest level where stellar crystals could be initiated corresponds to -12°C , and then these are transported by an updraft to the colder levels. Assuming the growth rate of $1\ \mu\text{m s}^{-1}$ at water saturation (Ryan et al. 1976) yields an assessment of the age of $300\text{-}\mu\text{m}$ stellar crystals as approximately 5 min. Playing back the growth time from the moment of observation of stellar crystals in Fig. 6a suggests that the level of origin of this crystal corresponds to the levels from approximately -13° to -14°C . This is consistent with the above assessment of the temperature of activation of INPs and the level of origin of first ice. There are also a few rimed stellars that reach sizes of $500\ \mu\text{m}$ in the penetrations at -16.5° and -17.6°C , which is consistent with the onset of riming of the pristine ice when it reached sizes in the hundreds of micrometers (Ono 1969; Baker and Lawson 2006).

RF06b (11 June 2021). The RF06b SPICULE mission took place in east-central Kansas. Figure 11a shows flight tracks of the two aircraft during the period of interest and Fig. 11b shows 1500 UTC 11 June and 0000 UTC 12 June 2021 soundings from Topeka, Kansas (TOP). Cloud-base elevation was $1,495\ \text{m}$ ($4,903\ \text{ft}$) at $850\ \text{mb}$. As seen in Fig. 11b, there was a strong inversion at $750\ \text{mb}$. Once the inversion was overcome convective bubbles experienced strong instability with a CAPE of $2,082\ \text{J kg}^{-1}$ on the 1500 UTC sounding, about 10 times the CAPE during both the RF04b mission ($202\ \text{J kg}^{-1}$) and the average ($197\ \text{J kg}^{-1}$) of the September 0000 UTC RPLI (Laoag) soundings during CAMP²Ex. The GV made a pass below cloud base from 2216:32 to 2217:10 UTC and measured the average PCASP aerosol concentration at $969\ \text{cm}^{-3}$ and average CN concentration at $2,310\ \text{cm}^{-3}$. The PCASP values are a factor of 1.9 higher than measured during RF04b, and the CN concentration is a factor of 1.4 higher. The T_{CB} was 22°C , which is close to the average $T_{\text{CB}} = 23^{\circ}\text{C}$ measured during the CAMP²Ex project. From 2226 to 2240 UTC the GV was held at $10,000\ \text{ft}$ ($3,049\ \text{m}$) by air traffic control and was not able to coordinate with the Learjet. Due to traffic, ATC vectored the Learjet southeast during this time period where it continued to sample CuCg.

Figure 12 shows photos, Lear KPR radar reflectivity, and particle images in a format similar to Fig. 6 for the RF04b case. Data from the 2D50 probe are not shown in Fig. 12 because only one millimeter drop was found among $60,150$ images in the cloud penetration at

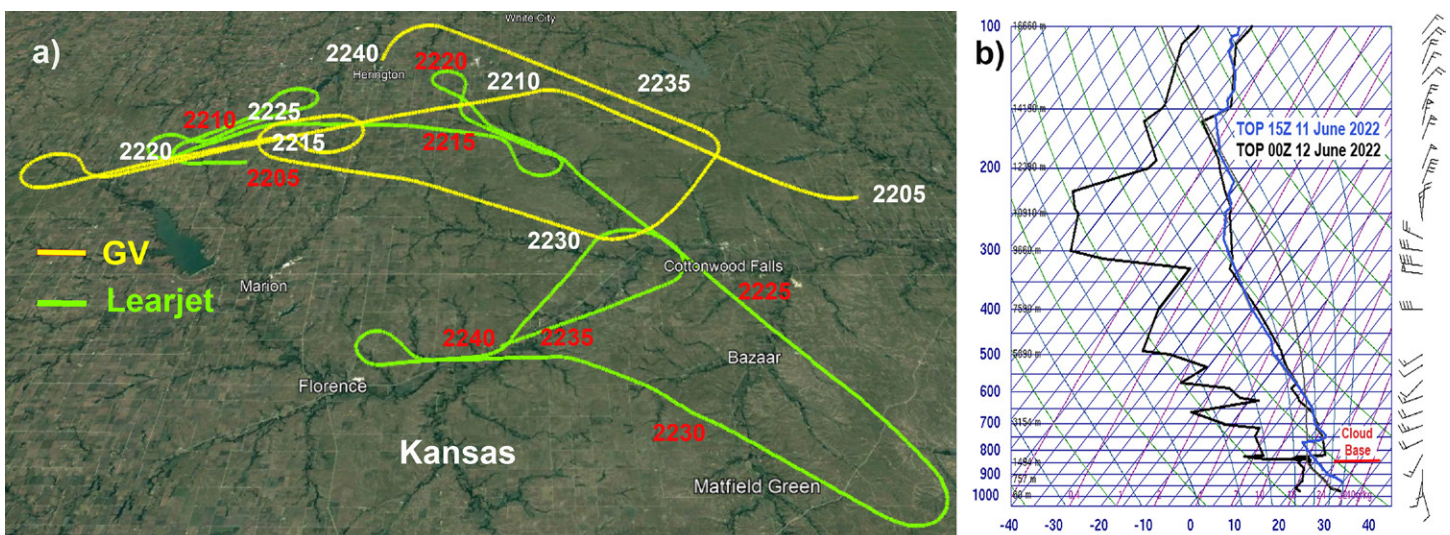


Fig. 11. (a) Portion of GV and Learjet flight tracks relevant to RF06b case study, and (b) Topeka (TOP) 1500 UTC 11 Jun and 0000 UTC 12 Jun 2021 soundings with an average CAPE of $2,082\ \text{J kg}^{-1}$.

-17.8°C. The radar reflectivity values are 10–20 dBZ lower than for the RF04b case, which is commensurate with the DSDs shown in Fig. 13a. The KPR reflectivity below ~2,000 m (~-15°C) was 10–20 dBZ lower compared to that during the RF04b flight. This is indicative of a lower intensity of the coalescence process and consequently lower concentration of precipitating drops during the cloud penetrations, which is supported by the DSDs shown in Fig. 13a.

The RF04b PSD measured at -17.6°C and shown in Figs. 9 and 13a contains an order of magnitude higher concentration of predominantly ice particles between 0.5 and 1 mm than does the RF06b DSD at -17.8°C. This is attributed to the rapid FFD SIP in the RF04b case that did not occur at the same temperature in the RF06b case. The R_{eff} measurements in Fig. 13b show a comparison of temperature versus R_{eff} for the RF04b and RF06b cases. The larger RF04b R_{eff} above the 0°C level supports the premise that the higher subcloud aerosol and cloud-base drop concentrations limited the coalescence process in the RF06b case. The very weak coalescence in the RF06b case compared with both the RF04b and CAMP²Ex cases is associated with two factors: the extremely high concentrations of subcloud aerosols and

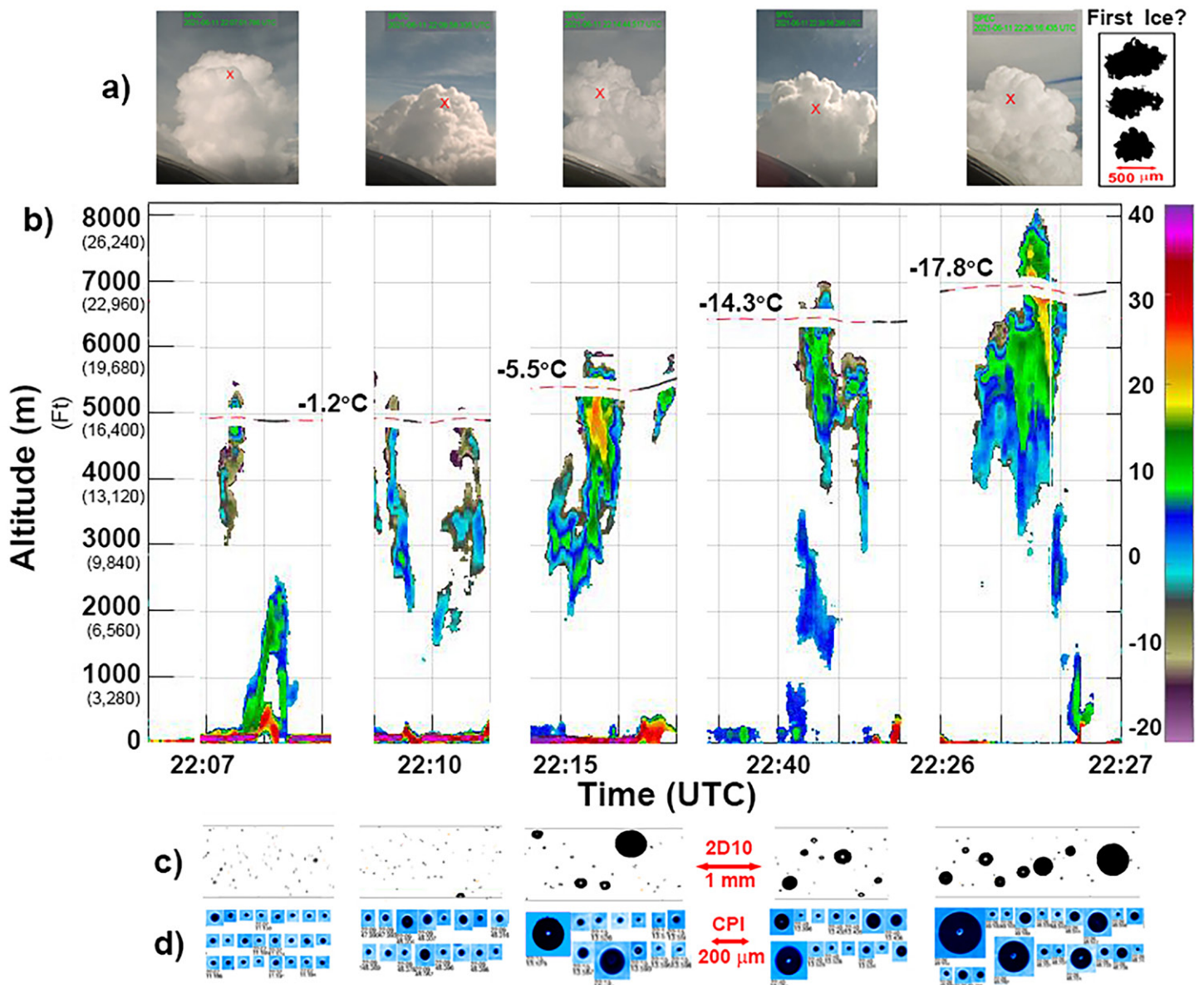


Fig. 12. RF06b measurements showing (a) photos of Learjet penetrations near cloud top (red X), (b) reflectivity measurements from the KPR radar, and examples of particle images from the (c) 2D10 and (d) CPI probes.

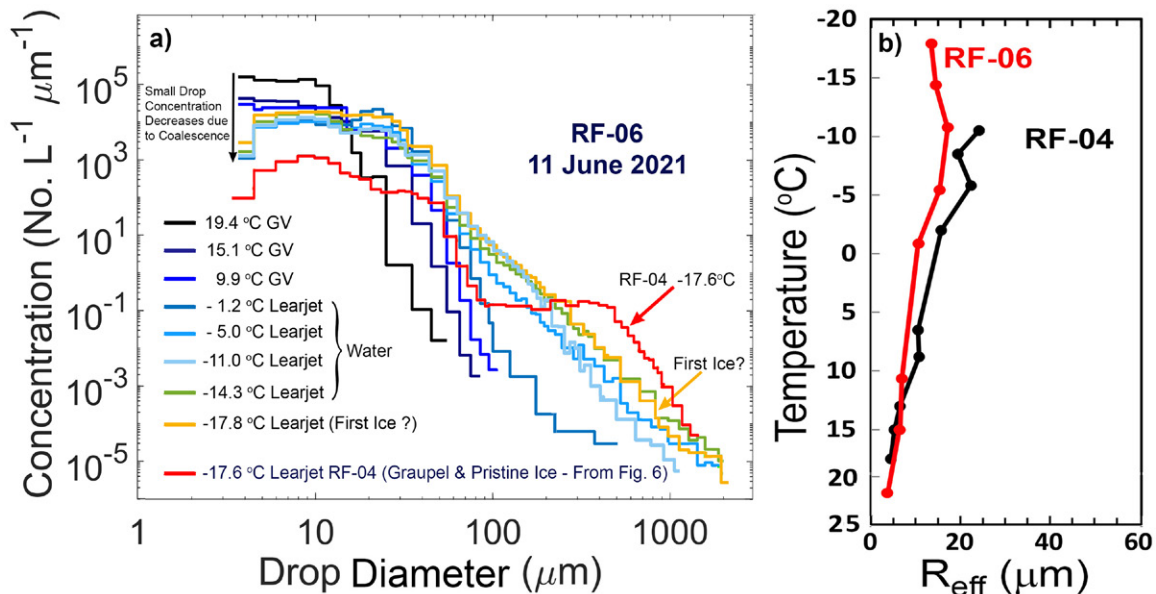


Fig. 13. (a) DSDs from GV and Learjet penetrations of ice-free updraft cores sampled in the RF06b case and (red) PSD from the RF04b case for comparison. The questionable first ice in the -17.8°C penetration is shown in Fig. 12 and discussed in the text. (b) Comparison of temperature vs R_{eff} plots for RF04b and RF06b.

drops at cloud base where 90% of the total drop concentration is in diameters $< 15 \mu\text{m}$, and the much higher CAPE in the RF06b case than either RF04b or CAMP²Ex (Figs. 3, 11, 12).

The CPI images do not contain any nonspherical images in any of the cloud penetrations shown in Fig. 12, suggesting a complete lack of measurable ice particles up to and including the -17.8°C cloud penetration. However, the 2D10 data did show three nonspherical images in 67,320 particle images, with 3,960 of the images $\geq 70 \mu\text{m}$, which is about the threshold for estimating sphericity. It is worth noting that at saturation over liquid, any ice particle $< 70 \mu\text{m}$ will grow beyond 100–200 μm within a few tens of seconds (Ryan et al. 1976) and become well detectable by CPI and 2D-S. This strengthens the conclusion that the concentration of ice particles was miniscule during the RF06b flight. Thus, all of the RF06b DSDs in Fig. 13a were essentially ice-free with the exception of the three nonspherical 2D10 images shown in the upper-right corner of Fig. 12.

We now focus on a discussion of whether these three images are the first detectable ice in these cloud penetrations. The first detectable images of ice particles in the RF04b case were larger and appeared to be frozen millimeter drops. However, with the scarcity of millimeter drops in the RF06b case it is likely that they may not be detected in the particle imagery. The three images are not pristine ice, but could have originated as smaller ice crystals that have rimed, or could be rimed fragments of larger drops. It is interesting to explore if these are consistent with understanding of primary nucleation in this case. Concentrations of INPs measured during RF06b suggest values consistent with or somewhat lower than in RF04b, with values of $< 0.1 \text{ L}^{-1}$ at -15°C and a broad range at times of $< 0.1\text{--}10 \text{ L}^{-1}$ at -20°C (Fig. 7). If the three nonspherical images in Fig. 12 are ice and are representative of first detectable ice in the RF06b case, they occurred in a concentration of about 0.1 L^{-1} , which is broadly consistent with the INP data in this case.

The main takeaway from the RF06b data is that in the absence of a strong coalescence process resulting in SLD production, the presence of a small concentration of ice particles (e.g., first ice in Fig. 12) is not sufficient to initiate the FFD SIP. Table 2 in L22 shows a high degree of correlation between ζ and the strength of the coalescence process in CuCg. However, in L22's Table 2 the mean cloud-base total drop concentration is 510 cm^{-3} , whereas the cloud-base total drop concentrations in the RF04b and RF06b cases are 922 and $1,388 \text{ cm}^{-3}$,

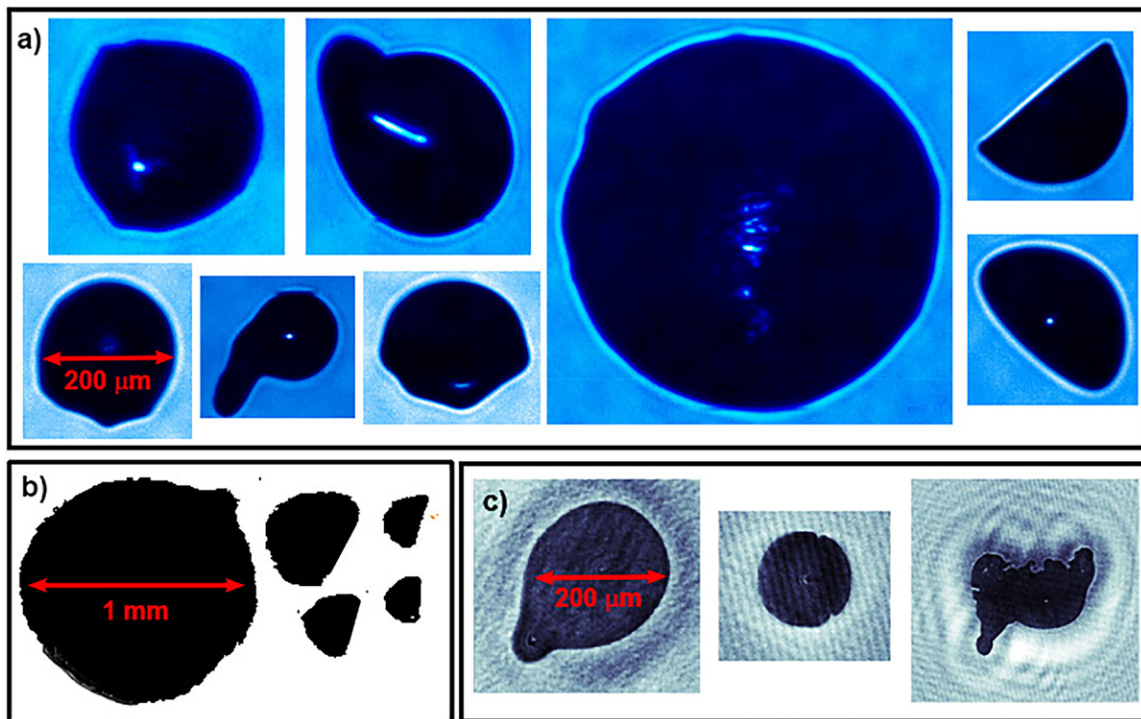


Fig. 14. Examples of images of fragments of frozen drops and frozen drops with protrusions from (a) CPI and (b) 2D-S probes on the Learjet in updraft cores from RF04b, and (c) HOLODEC probe on the GV in a downdraft at -3°C from RF06b. (HOLODEC images from Elise Rosky.)

respectively. This is consistent with 50%–200% higher PCASP aerosol concentrations ($>0.1\ \mu\text{m}$) and CN concentrations in the subcloud layer in RF06b versus RF04b. Recent modeling evidence shows that decreasing the subcloud aerosol concentration by a factor of 10 (from 618 to $62\ \text{cm}^{-3}$) increased the concentration of millimeter drops at the -12°C level in CuCg by an order of magnitude (Morrison et al. 2022). The RF04b and RF06b cases have similar T_{CB} values to the mean values from SEAC⁴RS and CAMP²Ex, respectively. However, the 50%–350% higher cloud-base drop concentrations in the SPICULE RF04b and RF06b cases appear to have significantly inhibited coalescence. The moderate coalescence in RF04b and very weak coalescence in RF06b led to initiation of FFD SIP observed at -16.5°C in RF04b, and no SIP in RF06b at the -17.8°C level. In contrast, strong coalescence was observed at the 0°C level in locations such as the Caribbean, South China, and Philippine Seas, which led to a very active SIP by the time updrafts reached the -12°C level (L22).

The influence of cloud-base aerosol and thus droplet concentration on the strength of coalescence, which leads to an active FFD SIP, is also apparent by examination of cloud-base drop concentrations in Fig. 4, and the plots of R_{eff} versus temperature in Figs. 5 and 14. As explained previously, several investigators have associated R_{eff} with an active coalescence process. The RF06b plot in Fig. 13b barely reaches a value of $17.4\ \mu\text{m}$ at -11°C , where the RF04b plot shows a value of $24.2\ \mu\text{m}$. In comparison, Fig. 5 shows that the SEAC⁴RS and CAMP²Ex mean R_{eff} values, which had similar T_{CB} values but significantly smaller values of cloud-base drop concentrations, were, respectively, $28\ \mu\text{m}$ at -6.5°C and $54.5\ \mu\text{m}$ at -3.0°C . This provides additional evidence that the strength of the coalescence process increases with increasing T_{CB} and DSD_{max} , and decreasing cloud-base drop concentration.

As noted above, an additional factor influencing the development of coalescence in the RF06b case is the much larger CAPE ($2,082\ \text{J kg}^{-1}$) compared with the RF04b case ($202\ \text{J kg}^{-1}$). The maximum vertical velocity measured in the RF04b was $9.2\ \text{m s}^{-1}$ and in the RF06b case it was $23.1\ \text{m s}^{-1}$ (Tables 3 and 4). Since the residence time of drops within a given depth of a convective updraft (i.e., the region with $T \geq 0^{\circ}\text{C}$) is inversely proportional to updraft velocity,

drop growth via coalescence will be less in stronger updrafts due to a fewer number of drop collision events, which to a first approximation, is proportional to time. Therefore, the stronger updraft in the RF06b case is another significant inhibitor to coalescence and FFD SIP at the observation levels.

Summary and discussion

The SPICULE project was designed and executed based on a series of previous aircraft investigations of CuCg by Lawson et al. (2015, 2017; L22). Results from these recent field campaigns shed new light on a hypothesized secondary ice process (SIP) that was introduced in the 1960s (e.g., Koenig 1963, 1965). As summarized by L22, a preponderance of evidence from five field campaigns in six geographic locations demonstrates that the SIP takes place in fresh updrafts of growing CuCg when some (yet undetermined) subset of supercooled large drops (SLDs) formed by collision–coalescence freeze and fracture in moderate-to-strong updraft cores of CuCg. The “fragmentation of freezing drops” (FFD) SIP process is hypothesized to produce frozen drop fragments and/or spicules that laboratory experiments show emit copious small ice particles (e.g., Wildeman et al. 2017). Figure 14 shows examples of fragments and protrusions of frozen drops from the two case studies in addition to images shown in Fig. 6. Note that ice that is hundreds of micrometers in size will rapidly rime in a mixed-phase environment so that the original ice particle or drop shape quickly becomes unrecognizable.

Here we discuss other SIP mechanisms that may potentially be active in cumulus clouds. Our preliminary analysis showed no evidence of the Hallett–Mossop (H-M) SIP mechanism (Hallett and Mossop 1974) near the cloud tops in the observed SPICULE clouds. The H-M process is active in a relatively narrow temperature range from -3° to -8°C . However, SPICULE observations showed that the rapid enhancement of the concentration of secondary ice particles occurred at temperatures colder than -10°C . This is well outside the temperature range where the H-M process can have any noticeable contribution on secondary ice concentrations. Nevertheless, the H-M process could be activated at a later stage in development, when recirculated secondary ice formed near cloud top is transported downward via downdrafts to the level from -3° to -8°C .

Activation of the following three SIP mechanisms related to 1) ice–ice collisional breakup, 2) fragmentation of sublimating ice, and 3) fragmentation of ice particles due to thermal shock requires the presence of a large number of diffusion grown ice and/or graupel in the same cloud volume (for details, see Korolev and Leisner 2020). Such a situation can occur at the mature stage of CuCg after the initial enhancement of the concentration of secondary ice and its spreading across the cloud.

Gagin (1972) proposed a SIP mechanism whereby INPs may be activated around freezing drops. However, in order to get a high supersaturation over ice ($>40\%$) to enhance the number of activated INPs around freezing drops, the air temperature should be colder than -20°C (e.g., Fukuta and Lee 1986; Chouippe et al. 2019). Such temperatures are colder than those measured in this study where the rapid enhancement of secondary ice concentration was observed. Therefore, out of six recognized SIP mechanisms, five of them can be ruled out in consideration of the initiation of SIP in SPICULE CuCg, and the first initiation of secondary ice production is most likely attributed to the FFD SIP process.

Results from SPICULE add further insight into the factors that influence the development of a strong coalescence process and the resulting SIP in CuCg, including both cloud dynamical and microphysical factors related to aerosols. Coordination between the NSF/NCAR GV and SPEC Learjet, both equipped with advanced microphysics instrumentation and up/down vertically pointing radars, add significant insight into the cloud microphysics and dynamics. This was the first application on the Learjet of the ProSensing Inc. Ka-band

up/down radar (KPR), on loan from Environment and Climate Change Canada. The KPR provided very valuable vertical profiles of the cloud structure as the Learjet penetrated near the tops of growing CuCg. The GV HIAPER Cloud Radar (HCR) added vertical profiles and microphysical measurements beneath the Learjet. Significant preliminary findings from SPICULE that include results from previous campaigns are as follows:

- The collision–coalescence process in cumulus congestus (CuCg) with moderate-to-strong ($5\text{--}20\text{ m s}^{-1}$) updraft cores is a function of the following cloud-base properties:
 - (i) Warm cloud-base temperature (T_{CB}): T_{CB} values from 10° to 25°C typically produce very weak to strong coalescence, respectively. CuCg with cloud-base temperatures $< 10^{\circ}\text{C}$ generally do not produce a coalescence process (L22).
 - (ii) Examples from SPICULE, SEAC⁴RS, and CAMP²Ex projects show that given similar T_{CB} values, coalescence is mitigated by narrow cloud-base DSDs with high total drop concentrations (L22).
 - (iii) DSDs at cloud base with diameters $< \sim 15\ \mu\text{m}$ appear to inhibit the coalescence process while drops from 15 to $30\ \mu\text{m}$ appear to enhance the coalescence process (Morrison et al. 2022; L22).
 - (iv) CuCg with cloud-base DSD_{max} that do not exceed $30\ \mu\text{m}$, such as found over the High Plains in the United States, rarely produce an active coalescence process (Heymsfield et al. 1979; L22).
- CuCg that produce a strong coalescence process (i.e., $\sim 1\text{ m}^{-3}$ millimeter-diameter drops at the 0°C level) generate an FFD SIP that rapidly facilitates freezing of the supercooled region of the updraft after primary initiation of first ice (Koenig 1963, 1965; L22). The comparative analysis of SPICULE RF04b and RF06b along with previous observations (Lawson et al. 2015, 2017; L22) suggest that the presence of SLDs is one of the necessary conditions for FFD SIP.
- The “first detectable ice” particles in updraft cores that do not appear to be contaminated by transport of ice from aloft, are not pristine, but instead the particle images reveal irregular shapes, which often appear to be large (from hundreds of micrometers to millimeters) frozen drops and rimed drop fragments (Lawson et al. 2015, 2017; L22).
- CuCg with very large CAPE (e.g., $> \sim 2,000\text{ J kg}^{-1}$) that produce strong updraft velocities ($15\text{--}25\text{ m s}^{-1}$), as in the RF06b case, reduce the time for coalescence to progress prior to the formation of ice and push the level of first ice formation to higher altitudes.
- The FFD SIP produced by a strong coalescence process, along with other factors such as riming and the Wegener–Bergeron–Findeisen process, results in rapid freezing and depletion of supercooled LWC. L22 have shown that there is about a 90% reduction of the (adiabatic) supercooled water by the -18°C level in clouds with $T_{\text{CB}} \geq \sim 20^{\circ}\text{C}$. In CuCg with moderate to weak coalescence, the level where the SIP and other factors freeze supercooled water increases with decreasing temperature (Lawson et al. 2017; L22). The RF06b SPICULE case provides an exception that may be due to a much higher concentration of subcloud aerosols and drop concentration at cloud base, and a very large CAPE.
- In CuCg where coalescence does not occur, primary nucleation appears to initiate freezing within the temperature range from about -15° to -20°C , but transport of ice downward along the edges of the updraft from colder regions aloft may introduce ice at warmer temperatures, which may result in the initiation of the H-M SIP process at levels from -3° to -8°C (Heymsfield et al. 1979; Dye et al. 1986; Moser and Lasher-Trapp 2017; L22) as well as other SIP mechanisms.

L22 has shown that coalescence and the FFD SIP in CuCg are a function of $\zeta = T_{CB} \times \text{DSD}_{\text{max}}$, where DSD_{max} is the maximum diameter of drops measured about 300 m above cloud base. Their results are germane to investigations in (weak to moderately polluted) locations with average cloud-base drop concentrations that were almost entirely in the range of 200–600 cm^{-3} , with the exception of studies over open ocean in the Caribbean, where the average cloud-base drop concentration was 89 cm^{-3} (Lawson et al. 2015). The SPICULE RF04b and RF06b case studies discussed here were conducted in locations with much higher cloud-base drop concentrations, 922 and 1,384 cm^{-3} , respectively. This is corroborated by Morrison et al. (2022), who reduced the concentration of the cloud-base aerosol concentration in a CuCg simulation from 612 to 61 cm^{-3} , and found an order of magnitude more millimeter-diameter drops at the 0°C level. This introduces another parameter, subcloud aerosol concentration and composition, which influences cloud-base drop concentration.

The subcloud aerosol and dynamical properties need to be incorporated into the ζ parameter to better determine the level aloft where LWC is depleted. In addition, environmental instability (CAPE) and temperature inversions aloft play a role in the dynamical evolution of CuCg and the level where coalescence and SIP are active. The interaction between the ambient aerosol population, coalescence, SIP, and the production of rain are also germane to simulations of intentional and inadvertent weather modification (Geresdi et al. 2021). These interactive factors may best be evaluated using sophisticated numerical simulations, preferably using Lagrangian particle-based microphysics and a “piggyback” scheme that isolates dynamics and microphysics (Grabowski 2015, 2020). The SPICULE dataset provides a wealth of data for testing our understanding of the relation between dynamic and microphysical factors and cloud evolution.

Acknowledgments. SPICULE was the first field campaign to be sponsored by the National Science Foundation in the 2020–21 COVID-19 era. We are extremely grateful to the NCAR Earth Observing Laboratory and Research Aviation Facility staff that safely managed the field campaign without a single COVID case that was attributable to exposure during the project. We would also like to acknowledge the skill and dedication of the Learjet pilots (Bill Harris and Joe LoRusso), and GV pilots (Scott McClain, Lee Baker, Boden LeMay, and Doug Stewart) who safely and effectively executed the flight patterns, and the cabin crews of each aircraft for operating the instrumentation. RPL, RTB, SW, and TS were supported primarily by NSF Award 1917510, with partial support from NASA Award 80NSSC18K0143 and from the National Center of Meteorology, Abu Dhabi, UAE, under the UAE Research Program for Rain Enhancement Science. PJD, RJP, RJP, KAM, and TCJH were supported by NSF Award 1917519. KAM also acknowledges support by an NSF Graduate Research Fellowship under Grant 006784. The National Center for Atmospheric Research is sponsored by the National Science Foundation.

Data availability statement. All SPICULE data are archived at <https://data.eol.ucar.edu/>.

References

- Andreae, M. D., D. Rosenfeld, P. Artaxo, A. A. Costa, G. P. Frank, K. M. Longo, and M. A. F. Silva-Dias, 2004: Smoking rain clouds over the Amazon. *Science*, **303**, 1337–1342, <https://doi.org/10.1126/science.1092779>.
- Baker, B. A., and R. P. Lawson, 2006: In situ observations of the microphysical properties of wave, cirrus, and anvil clouds. Part I: Wave clouds. *J. Atmos. Sci.*, **63**, 3160–3185, <https://doi.org/10.1175/JAS3802.1>.
- Barry, K. R., and Coauthors, 2021: Observations of ice nucleating particles in the free troposphere from western US wildfires. *J. Geophys. Res. Atmos.*, **126**, e2020JD033752, <https://doi.org/10.1029/2020JD033752>.
- Blyth, A. M., W. A. Cooper, and J. B. Jensen, 1988: A study of the source of entrained air in Montana cumuli. *J. Atmos. Sci.*, **45**, 3944–3964, [https://doi.org/10.1175/1520-0469\(1988\)045<3944:ASOTSO>2.0.CO;2](https://doi.org/10.1175/1520-0469(1988)045<3944:ASOTSO>2.0.CO;2).
- Braham, R. R., Jr., 1964: What is the role of ice in summer rain showers? *J. Atmos. Sci.*, **21**, 640–645, [https://doi.org/10.1175/1520-0469\(1964\)021<0640:WITROI>2.0.CO;2](https://doi.org/10.1175/1520-0469(1964)021<0640:WITROI>2.0.CO;2).
- Byers, H. R., and R. R. Braham, 1949: *The Thunderstorm*. U.S. Government Printing Office, 287 pp.
- Cai, Y., J. R. Snider, and P. Wechsler, 2013: Calibration of the passive cavity aerosol spectrometer probe for airborne determination of the size distribution. *Atmos. Meas. Tech.*, **6**, 2349–2358, <https://doi.org/10.5194/amt-6-2349-2013>.
- Chouippe, A., M. Kraymer, M. Uhlmann, J. Dusek, A. Kiselev, and T. Leisner, 2019: Heat and water vapor transfer in the wake of a falling ice sphere and its implication for secondary ice formation in clouds. *New J. Phys.*, **21**, 043043, <https://doi.org/10.1088/1367-2630/ab0a94>.
- DeMott, P. J., and Coauthors, 2017: Comparative measurements of ambient atmospheric concentrations of ice nucleating particles using multiple immersion freezing methods and a continuous flow diffusion chamber. *Atmos. Chem. Phys.*, **17**, 11 227–11 245, <https://doi.org/10.5194/acp-17-11227-2017>.
- Dye, J. E., and Coauthors, 1986: Early electrification and precipitation development in a small, isolated Montana cumulonimbus. *J. Geophys. Res.*, **91**, 1231–1247, <https://doi.org/10.1029/JD091iD01p01231>.
- Field, P. R., and A. J. Heymsfield, 2015: Importance of snow to global precipitation. *Geophys. Res. Lett.*, **42**, 9512–9520, <https://doi.org/10.1002/2015GL065497>.
- , and Coauthors, 2017: Secondary ice production: Current state of the science and recommendations for the future. *Ice Formation and Evolution in Clouds and Precipitation: Measurement and Modeling Challenges*, Meteor. Monogr., No. 58, Amer. Meteor. Soc., <https://doi.org/10.1175/AMSMONOGRAPHS-D-16-0014.1>.
- Fletcher, N. H., 1962: *The Physics of Rain Clouds*. Cambridge University Press, 390 pp.
- Freud, E., and D. Rosenfeld, 2012: Linear relation between convective cloud drop number concentration and depth for rain initiation. *J. Geophys. Res.*, **117**, D02207, <https://doi.org/10.1029/2011JD016457>.
- Fukuta, N., and H. J. Lee, 1986: A numerical study of the supersaturation field around growing graupel. *J. Atmos. Sci.*, **43**, 1833–1843, [https://doi.org/10.1175/1520-0469\(1986\)043<1833:ANSOTS>2.0.CO;2](https://doi.org/10.1175/1520-0469(1986)043<1833:ANSOTS>2.0.CO;2).
- Gagin, A., 1972: Effect of supersaturation on the ice crystal production by natural aerosols. *J. Rech. Atmos.*, **6**, 175–185.
- Gerber, H., 1996: Microphysics of marine stratocumulus clouds with two drizzle modes. *J. Atmos. Sci.*, **53**, 1649–1662, [https://doi.org/10.1175/1520-0469\(1996\)053<1649:MOMSCW>2.0.CO;2](https://doi.org/10.1175/1520-0469(1996)053<1649:MOMSCW>2.0.CO;2).
- Geresdi, I., and Coauthors, 2021: Impact of hygroscopic seeding on the initiation of precipitation formation: Results of a hybrid bin microphysics parcel model. *Atmos. Chem. Phys.*, **21**, 16 143–16 159, <https://doi.org/10.5194/acp-21-16143-2021>.
- Grabowski, W. W., 2015: Untangling microphysical impacts on deep convection applying a novel modeling methodology. *J. Atmos. Sci.*, **72**, 2446–2464, <https://doi.org/10.1175/JAS-D-14-0307.1>.
- , 2020: Comparison of Eulerian bin and Lagrangian particle-based microphysics in simulations of nonprecipitating cumulus. *J. Atmos. Sci.*, **77**, 3951–3970, <https://doi.org/10.1175/JAS-D-20-0100.1>.
- Hallett, J., and S. C. Mossop, 1974: Production of secondary ice particles during the riming process. *Nature*, **249**, 26–28, <https://doi.org/10.1038/249026a0>.
- Heymsfield, A., and P. Willis, 2014: Cloud conditions favoring secondary ice particle production in tropical maritime convection. *J. Atmos. Sci.*, **71**, 4500–4526, <https://doi.org/10.1175/JAS-D-14-0093.1>.
- , C. A. Knight, and J. E. Dye, 1979: Ice initiation in unmixed updraft cores in northeastern Colorado cumulus congestus clouds. *J. Atmos. Sci.*, **36**, 2216–2229, [https://doi.org/10.1175/1520-0469\(1979\)036<2216:IIUUC>2.0.CO;2](https://doi.org/10.1175/1520-0469(1979)036<2216:IIUUC>2.0.CO;2).
- , G. Thompson, H. Morrison, A. Bansemer, R. M. Rasmussen, P. Minnis, Z. Wang, and D. Zhang, 2011: Formation and spread of aircraft-induced holes in clouds. *Science*, **333**, 77–81, <https://doi.org/10.1126/science.1202851>.
- Hobbs, P. V., 1969: Ice multiplication in clouds. *J. Atmos. Sci.*, **26**, 315–318, [https://doi.org/10.1175/1520-0469\(1969\)026<0315:IMIC>2.0.CO;2](https://doi.org/10.1175/1520-0469(1969)026<0315:IMIC>2.0.CO;2).
- , and A. L. Rangno, 1990: Rapid development of high ice particle concentrations in small polar maritime cumuliform clouds. *J. Atmos. Sci.*, **47**, 2710–2722, [https://doi.org/10.1175/1520-0469\(1990\)047<2710:RDOHIP>2.0.CO;2](https://doi.org/10.1175/1520-0469(1990)047<2710:RDOHIP>2.0.CO;2).
- Johnson, D. B., 1982: The role of giant and ultragiant aerosol particles in warm rain initiation. *J. Atmos. Sci.*, **39**, 448–460, [https://doi.org/10.1175/1520-0469\(1982\)039<0448:TROGAU>2.0.CO;2](https://doi.org/10.1175/1520-0469(1982)039<0448:TROGAU>2.0.CO;2).
- Keinert, A., D. Spannagel, T. Leisner, and A. Kiselev, 2020: Secondary ice production upon freezing of freely falling drizzle droplets. *J. Atmos. Sci.*, **77**, 2959–2967, <https://doi.org/10.1175/JAS-D-20-0081.1>.
- King, W. D., D. A. Parkin, and R. J. Handsworth, 1978: A hot-wire liquid water device having fully calculable response characteristics. *J. Appl. Meteor.*, **17**, 1809–1813, [https://doi.org/10.1175/1520-0450\(1978\)017<1809:AHWLWD>2.0.CO;2](https://doi.org/10.1175/1520-0450(1978)017<1809:AHWLWD>2.0.CO;2).
- Koenig, L. R., 1963: The glaciating behavior of small cumulonimbus clouds. *J. Atmos. Sci.*, **20**, 29–47, [https://doi.org/10.1175/1520-0469\(1963\)020<0029:TGBOSC>2.0.CO;2](https://doi.org/10.1175/1520-0469(1963)020<0029:TGBOSC>2.0.CO;2).
- , 1965: Drop freezing through drop breakup. *J. Atmos. Sci.*, **22**, 448–451, [https://doi.org/10.1175/1520-0469\(1965\)022<0448:DFTDB>2.0.CO;2](https://doi.org/10.1175/1520-0469(1965)022<0448:DFTDB>2.0.CO;2).
- Korolev, A., and T. Leisner, 2020: Review of experimental studies of secondary ice production. *Atmos. Chem. Phys.*, **20**, 11 767–11 797, <https://doi.org/10.5194/acp-20-11767-2020>.
- , J. W. Strapp, G. A. Isaac, and A. N. Nevzorov, 1998: The Nevzorov airborne hot-wire LWC–TWC probe: Principle of operation and performance characteristics. *J. Atmos. Oceanic Technol.*, **15**, 1495–1510, [https://doi.org/10.1175/1520-0426\(1998\)015<1495:TNAHWL>2.0.CO;2](https://doi.org/10.1175/1520-0426(1998)015<1495:TNAHWL>2.0.CO;2).
- , E. F. Emery, J. W. Strapp, S. G. Cober, and G. A. Isaac, 2013: Quantification of the effects of shattering on airborne ice particle measurements. *J. Atmos. Oceanic Technol.*, **30**, 2527–2553, <https://doi.org/10.1175/JTECH-D-13-00115.1>.
- , and Coauthors, 2020: A new look at the environmental conditions favorable to secondary ice production. *Atmos. Chem. Phys.*, **20**, 1391–1429, <https://doi.org/10.5194/acp-20-1391-2020>.
- Lance, S., 2012: Coincidence errors in a cloud droplet probe (CDP) and a cloud and aerosol spectrometer (CAS), and the improved performance of a modified CDP. *J. Atmos. Oceanic Technol.*, **29**, 1532–1541, <https://doi.org/10.1175/JTECH-D-11-00208.1>.
- Lauber, A., A. Kiselev, T. Pander, P. Handmann, and T. Leisner, 2018: Secondary ice formation during freezing of levitated droplets. *J. Atmos. Sci.*, **75**, 2815–2826, <https://doi.org/10.1175/JAS-D-18-0052.1>.
- Lawson, R. P., 2011: Effects of ice particles shattering on the 2D-S probe. *Atmos. Meas. Tech.*, **4**, 1361–1381, <https://doi.org/10.5194/amt-4-1361-2011>.
- , R. E. Stewart, and L. J. Angus, 1998: Observations and numerical simulations of the origin and development of very large snowflakes. *J. Atmos. Sci.*, **55**, 3209–3229, [https://doi.org/10.1175/1520-0469\(1998\)055<3209:OANSOT>2.0.CO;2](https://doi.org/10.1175/1520-0469(1998)055<3209:OANSOT>2.0.CO;2).

- , B. A. Baker, C. G. Schmitt, and T. L. Jensen, 2001: An overview of microphysical properties of Arctic clouds observed in May and July during FIRE ACE. *J. Geophys. Res.*, **106**, 14989–15014, <https://doi.org/10.1029/2000JD900789>.
- , D. O'Connor, P. Zmarzly, K. Weaver, B. Baker, Q. Mo, and H. Jonsson, 2006: The 2D-S (Stereo) probe: Design and preliminary tests of a new airborne, high speed, high-resolution particle imaging probe. *J. Atmos. Oceanic Technol.*, **23**, 1462–1477, <https://doi.org/10.1175/JTECH1927.1>.
- , S. Woods, and H. Morrison, 2015: The microphysics of ice and precipitation development in tropical cumulus clouds. *J. Atmos. Sci.*, **72**, 2429–2445, <https://doi.org/10.1175/JAS-D-14-0274.1>.
- , C. Gurganus, S. Woods, and R. Brientjes, 2017: Aircraft observations of cumulus microphysics ranging from the tropics to midlatitudes: Implications for a “new” secondary ice process. *J. Atmos. Sci.*, **74**, 2899–2920, <https://doi.org/10.1175/JAS-D-17-0033.1>.
- , R. Brientjes, S. Woods, and C. Gurganus, 2022: Coalescence and secondary ice production in cumulus congestus clouds. *J. Atmos. Sci.*, **79**, 953–972, <https://doi.org/10.1175/JAS-D-21-0188.1>.
- Levin, E. J. T., and Coauthors, 2019: Characteristics of ice nucleating particles in and around California winter storms. *J. Geophys. Res. Atmos.*, **124**, 11 530–11 551, <https://doi.org/10.1029/2019JD030831>.
- Matrosov, S., A. Heymsfield, and Z. Wang, 2005: Dual-frequency radar ratio of nonspherical atmospheric hydrometeors. *Geophys. Res. Lett.*, **32**, L13816, <https://doi.org/10.1029/2005GL023210>.
- Morrison, H., J. Peters, A. C. Varble, W. M. Hannah, and S. E. Giangrande, 2020: Thermal chains and entrainment in cumulus updrafts. Part I: Theoretical description. *J. Atmos. Sci.*, **77**, 3637–3660, <https://doi.org/10.1175/JAS-D-19-0243.1>.
- , P. Lawson, and K. K. Chandaker, 2022: Observed and bin model simulated evolution of drop size distributions in high-based cumulus congestus over the United Arab Emirates. *J. Geophys. Res. Atmos.*, **127**, e2021JD035711, <https://doi.org/10.1029/2021JD035711>.
- Moser, D. H., and S. Lasher-Trapp, 2017: The influence of successive thermals on entrainment and dilution in a simulated cumulus congestus. *J. Atmos. Sci.*, **74**, 375–392, <https://doi.org/10.1175/JAS-D-16-0144.1>.
- O'Connor, D., B. Baker, and R. P. Lawson, 2008: Upgrades to the FSSP-100 electronics. *Int. Conf. on Clouds and Precipitation*, Cancun, Mexico, IAMAS, http://convention-center.net/iccp2008/abstracts/Program_on_line/Poster_13/OConnor_extended_final.pdf.
- Ono, A., 1969: The shape and riming properties of ice crystals in natural clouds. *J. Atmos. Sci.*, **26**, 138–147, [https://doi.org/10.1175/1520-0469\(1969\)026<0138:TSARPO>2.0.CO;2](https://doi.org/10.1175/1520-0469(1969)026<0138:TSARPO>2.0.CO;2).
- Phillips, V. T. J., S. Patade, J. Gutierrez, and A. Bansemer, 2018: Secondary ice production by fragmentation of freezing drops: Formulation and theory. *J. Atmos. Sci.*, **75**, 3031–3070, <https://doi.org/10.1175/JAS-D-17-0190.1>.
- Pinsky, M., A. Khain, and M. Shapiro, 2001: Collision efficiency of drops in a wide range of Reynolds numbers: Effects of pressure on spectrum evolution. *J. Atmos. Sci.*, **58**, 742–764, [https://doi.org/10.1175/1520-0469\(2001\)058<0742:CEODIA>2.0.CO;2](https://doi.org/10.1175/1520-0469(2001)058<0742:CEODIA>2.0.CO;2).
- Pruppacher, H. R., and J. D. Klett, 1997: *Microphysics of Clouds and Precipitation*. Kluwer Academic, 954 pp.
- Rangno, A. L., and P. V. Hobbs, 1983: Production of ice particles in clouds due to aircraft penetrations. *J. Climate Appl. Meteor.*, **22**, 214–232, [https://doi.org/10.1175/1520-0450\(1983\)022<0214:POIPIC>2.0.CO;2](https://doi.org/10.1175/1520-0450(1983)022<0214:POIPIC>2.0.CO;2).
- Roberts, G., and A. A. Nenes, 2005: Continuous-flow streamwise thermal-gradient CCN chamber for atmospheric measurements. *Aerosol Sci. Technol.*, **39**, 206–221, <https://doi.org/10.1080/027868290913988>.
- Rosenfeld, D., and G. Gutman, 1994: Retrieving microphysical properties near the tops of potential rain clouds by multispectral analysis of AVHRR data. *Atmos. Res.*, **34**, 259–283, [https://doi.org/10.1016/0169-8095\(94\)90096-5](https://doi.org/10.1016/0169-8095(94)90096-5).
- Ryan, B. F., E. R. Wishart, and D. E. Shaw, 1976: The growth rates and densities of ice crystals between -3°C and -21°C . *J. Atmos. Sci.*, **33**, 842–850, [https://doi.org/10.1175/1520-0469\(1976\)033<0842:TGRADO>2.0.CO;2](https://doi.org/10.1175/1520-0469(1976)033<0842:TGRADO>2.0.CO;2).
- Spuler, S. M., and J. Fugal, 2011: Design of an in-line, digital holographic imaging system for airborne measurement of clouds. *Appl. Opt.*, **50**, 1405–1412, <https://doi.org/10.1364/AO.50.001405>.
- Squires, P., 1958: The microstructure and colloidal stability of warm clouds. *Tellus*, **10**, 256–261, <https://doi.org/10.3402/tellusa.v10i2.9229>.
- Twohy, C. H., and Coauthors, 2016: Abundance of fluorescent biological aerosol particles at temperatures conducive to the formation of mixed-phase and cirrus clouds. *Atmos. Chem. Phys.*, **16**, 8205–8225, <https://doi.org/10.5194/acp-16-8205-2016>.
- Vardiman, L., 1978: The generation of secondary ice particles in clouds by crystal–crystal collision. *J. Atmos. Sci.*, **35**, 2168–2180, [https://doi.org/10.1175/1520-0469\(1978\)035<2168:TGOSIP>2.0.CO;2](https://doi.org/10.1175/1520-0469(1978)035<2168:TGOSIP>2.0.CO;2).
- Vonnegut, B., 1947: The nucleation of ice formation by silver iodide. *J. Appl. Phys.*, **18**, 593–595, <https://doi.org/10.1063/1.1697813>.
- Wildeman, S., S. Sterl, C. Sun, and D. Lohse, 2017: Fast dynamics of water droplets freezing from the outside in. *Phys. Rev. Lett.*, **118**, 084101, <https://doi.org/10.1103/PhysRevLett.118.084101>.
- Woods, S., P. Lawson, E. Jensen, T. Thornberry, A. Rollins, P. Bui, L. Pfister, and M. Avery, 2018: Microphysical properties of tropical tropopause layer cirrus. *J. Geophys. Res. Atmos.*, **123**, 6053–6069, <https://doi.org/10.1029/2017JD028068>.